Masterarbeit

Construction and setup of a 3rd generation Rydberg Quantum Optics experiment

Florian Christaller

20. October 2017

5. Physikalisches Institut

Stuttgart
Universität

Hauptberichter: Prof. Dr. Sebastian Hofferberth
Prof. Dr. Tilman Pfau
Mitberichter: Prof. Dr. Peter Michler

Zusammenfassung

In dieser Arbeit wird der Wiederaufbau des Rydberg Quanten Optik Experiments, nach einem Umzug von Stuttgart nach Odense, beschrieben. Im Zuge dessen wurde der Aufbau des Lasertisches neu gestaltet. Zudem wurde ein besseres Laser Stabilisierungssystem verwendet, der sogenannte digitale Phasen-Lock. Der bestehende optische Referenzresonator wurde nach dem Umzug charakterisiert. Um für eine ausreichende Menge an Rubidium in der Vakuum Kammer zu sorgen, wurde eine neue Halterung erstellt, welche drei Paare von Rubidium Spendern beinhaltet. Mit einem neuen Optik Board oberhalb der Glaszelle kann ein neues Abbildungssystem verwendet werden. Das Objektiv des neuen vertikalen Abbildungssystem wurde mit Hilfe einer Auflösungstesttafel charakterisiert.

Abstract

This thesis describes the reconstruction of the Rydberg quantum optics experiment, after a move from Stuttgart to Odense. In the course of this the setup of the laser table was redesigned. In addition, a better laser stabilization system was used, the so-called digital phase lock. The existing optical reference cavity was characterized after the move. In order to provide a sufficient amount of Rubidium in the vacuum chamber, a new holder was created which includes three pairs of Rubidium dispensers. A new imaging system can be used with a new optics board above the glass cell. The objective of the new vertical imaging system was characterized with a resolution test chart.

Declaration

I hereby declare that this submission is my own work and that, to the best of my knowledge and belief, it contains no material previously published or written by a nother person, except where due acknowledgment has been made in the text.

Stuttgart, 20. October 2017
Florian Christaller

Contents

1 Introduction

The field of nonlinear quantum optics is a still growing topic. The goal is to build optical networks with communication on the single photon level. A prominent example for quantum optics is Rydberg quantum optics [1, 2, 3], where Rydberg atoms [4] mediate interactions between photons. Those Rydberg atoms are excited atoms, where normally one electron is at a high principal quantum number.
There are many systems to study Rydberg states and their interaction with photons. Among these are recent experiments in hot atomic gases [5, 6, 7], or even naturally grown crystals of cuprous oxide [8].
An ideal candidate to study the strong interactions between individual Rydberg atoms are ultra cold atomic gases. Here, the negligible Doppler-shift in the excitation scheme of Rydberg states manifests large blockade radii [9] on the order of several micro meter. Within this so-called Rydberg blockade, the excitation of a second atom into the Rydberg sate is energetically forbidden. By choosing an appropriate principal quantum number, the interaction strength and therefore the size of the blockade radius can be tuned over a wide range. Mapping these interactions onto individual photons allows to engineer a highly nonlinear system, where both the phase and the amplitude of transmitted light can be altered photon by photon [2, 10, 11] and fundamental building blocks for purely photonic quantum applications can be realized [12, 13]. The strength of the achievable interaction in such Rydberg based systems is comparable to other approaches as atomic ensembles in cavities [14], emitters coupled to waveguides [15, 16, 17], or single atoms which are coupled to light in free space [18].

Our experiment contains a cloud of ultra cold atoms, which is addressable with Rydberg excitation and probe lasers. In our experiment we can have different scenarios. With a large cold atom cloud and a low Rydberg state we can have several Rydberg atoms in our cloud. In this configuration we use the effect of the electromagnetically induced transparency (EIT) to implement for example the single photon transistor [13]. The other scenario is a small atom cloud and a high Rydberg state, such that only a single Rydberg atom can be excited, which blocks the cloud. That kind of Rydberg atom can be described with a model called superatom. In this configuration we measured the single photon absorber [19].
The first version of our Rydberg Quantum Optics (RQO) experiment was setup in 2012. After two years the apparatus was modified. The main change was a new electric field control for the second generation RQO experiment. During my master thesis the experiment moved from Stuttgart to Odense and thereby was modified again. The current setup is the third generation RQO experiment. The last data, measured with the second generation, were the observation of the "Free-Space Quantum Electrodynamics with a Single Rydberg Superatom" [20] and the "Electromagnetically induced transparency of ultra-long-range Rydberg molecules" [21].

In this thesis I will describe the changes from the second to the third generation RQO experiment. As it is not possible to write down every single step of the move, I will focus on a few main projects in my master thesis. These are among others a new laser stabilization system, a new holder for the in vacuum Rubidium dispenser and a new vertical imaging setup. Next to this I describe the rebuild of the laser- and experiment-table, which are the two components of the RQO experiment.

2 Lab Infrastructure

The move from Stuttgart to Odense gave the opportunity to set up the experiment from scratch. The Rydberg quantum optics (RQO) experiment version 3.0 in Odense is based on the setup in Stuttgart, version 2.0. It was among others my job to plan and carry out the move of the experiment.
This chapter deals with the move of the experiment to Odense and the design of the new lab.

2.1 Chronological Sequence of the Move

The scheduling of the move from Stuttgart to Odense started at the end of the year 2016. We had to plan what equipment we need as a new physics group in Odense. In Stuttgart we used the equipment shared with other groups at the 5. physical institute, in Odense we need our own equipment. This starts with simple tools as screwdrivers or a soldering station and continues with electrical cables and oscilloscopes. For our new group in Odense we had to buy all that equipment.
At the beginning of March 2017 I visited the new lab for the first time. The almost empty room was renovated for us and had several desks and shelves. Also power connectors and outlets for cooling water were already installed. The first thing I did was a plan of where to place the optical tables. In addition to the two optical tables from Stuttgart we got two new tables. The four tables are positioned such that one can comfortably work on them.
In mid-March, we disassembled the experiment in Stuttgart. So all the optics on the optical tables had to be dismantled and all the electronics and cables had to be packed in boxes. For the optics we used portable aluminum boards with threads to screw the optics on them. For the vacuum chamber we also had an aluminum board with a construction to protect the glass cell of the vacuum chamber.
At the end of March a moving company packed our stuff in Stuttgart and brought it to Odense. There they placed the four optical tables at the marked positions and unloaded our stuff. From now on we started with the reconstruction.

In the following sections I describe the main parts of the reconstruction and also focus on changes and new parts of the RQO experiment version 3.0.

2.2 Lab Layout

As mentioned before, we have four optical tables. Two of them we use for the experiment from Stuttgart, the other two are for a new experiment in the future. From now on, I will only talk about the reconstruction of the experiment from Stuttgart.
The experiment consists of two optical tables, one is the laser-table and the other is the experiment-table. On the laser-table we have all lasers, except one high power laser, which is placed on the experiment-table. On the experiment-table we have our vacuum chamber. Both tables are framed by a rack made of *Rose+Krieger* aluminum profiles.

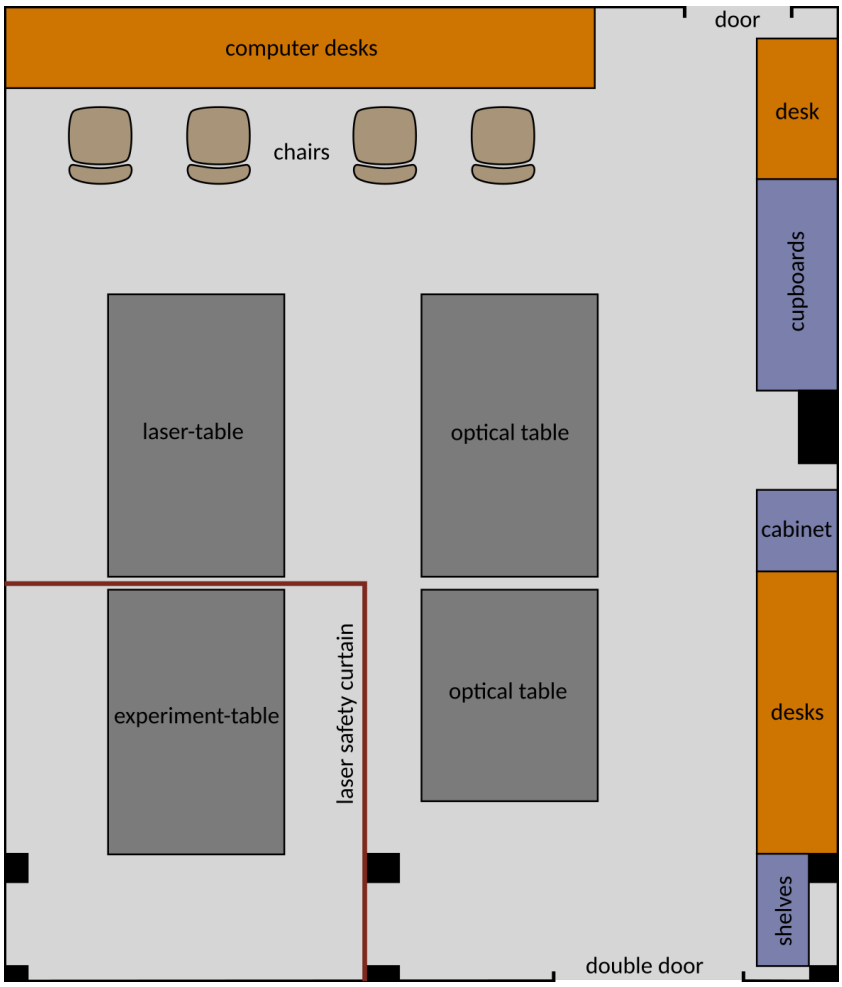

Figure 2.1: Floor plan of the new lab in Odense. The optical tables are shown in dark gray. Our storage space is marked in dark blue. We also have shelves on the walls above the desks, shown in orange. The laser safety curtain, marked in dark red, surrounds the experiment-table with the high power laser.

Those racks have two levels of shelves above the tables for the electrical devices, which control the lasers and the experiment. The racks are also used to attach covers around the tables. Because of the high power laser, the experiment-table is covered additionally by a laser safety curtain. That laser safety curtain is also mounted on the rack.

A scheme of the lab is shown in Figure 2.1. The RQO experiment is on the two tables labeled "laser-table" and "experiment-table". These two tables are discussed in more detail in section 3 and in section 4. The other two optical tables were used for small side-projects until now.

2.3 RQO Experiment

The purpose of the Rydberg quantum optics (RQO) experiment is to map the strong interaction among individual Rydberg atoms onto photons to create highly nonlinear

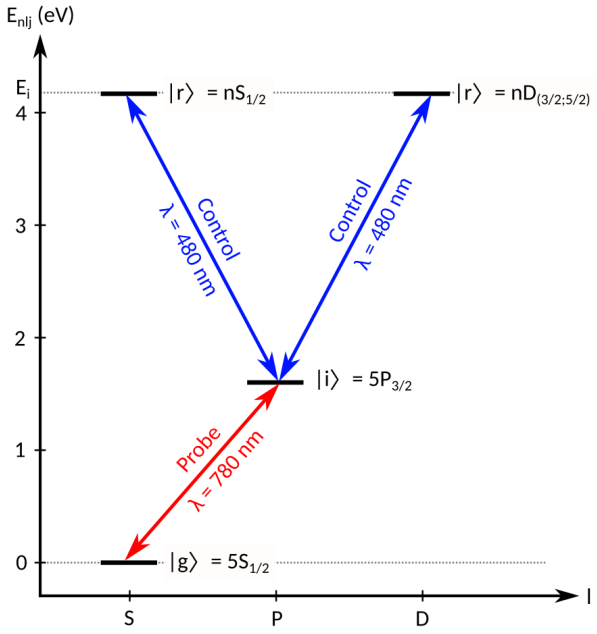

Figure 2.2: Rydberg excitation scheme for Rubidium atoms. The Rubidium atoms in the ground state $|g\rangle = 5S_{1/2}$ can be excited to the intermediate state $|i\rangle = 5P_{3/2}$ via the probe laser at 780 nm. From the intermediate state the control laser at 480 nm can couple to a Rydberg state $|r\rangle = nS_{1/2}$ or $|r\rangle = nD_{3/2;5/2}$, where the principal quantum number is in the range $n = 40 - 121$.

medium. Due to a enhanced coupling between light and matter we can observe effective photon-photon interactions. Therefore we use Rubidium atoms in ultra high vacuum, which were cooled by different steps of laser cooling. In the cloud of ultra cold atoms we excite single atoms into a Rydberg state. The Rydberg excitation is done by the absorption of two photons, one red photon at 780 nm and one blue photon at 480 nm. The excitation scheme is shown in Figure 2.2. The ground state $|g\rangle$ Rubidium atom is excited into an intermediate state $|i\rangle$ by absorbing a red photon. From the intermediate state the atom reaches a Rydberg state $|r\rangle$, with principal quantum number $n = 40 - 121$, by absorbing a blue photon. The red transition is called "Probe" because we measure the out coming photons of that transition. The blue transition is the "Control" transition with which we enable or disable the excitation and stimulated emission of the Rydberg state.

Those Rydberg atoms have the property to blockade a certain volume around itself, where no other atom can be excited into a Rydberg state. That so called Rydberg blockade in combination with a small atom cloud, leads to an atom cloud, where only a few excitations can exist. By sending only a few photons into the atom cloud, we can observe strong nonlinear optical effects on the few photon level in the cloud.
A more detailed description of the experiment can be read in the dissertations of H. Gorniaczyk [22] and C. Tresp [23].

3 Laser-table Setup

One of the first things we rebuilt in Odense was the laser-table. I was essentially involved in the setup of the optics on the laser-table.
In this chapter I present the new layout of the laser-table and two sections of it in detail. One is the digital phase lock, which we use to stabilize our lasers, and the other is the reconstruction and characterization of the optical reference cavity.

3.1 Laser-table Layout

The laser-table is one of the main parts of the RQO experiment. There we have our lasers and optics to control and stabilize both frequency and power of each individual laser. The optical elements to control the lasers are described in subsubsection 3.1.2 and the usage of each laser is described in subsubsection 3.1.1.

The layout of the laser-table in Odense is completely new compared to Stuttgart. Now we have some new lasers and also a bigger optical table. As we use the technique to stabilize most of our laser with respect to a master laser, we had to set them up such that the light of the master laser is the central beam. All other lasers are set up along the central beam of the master laser. The master laser is in turn stabilized with a reference cavity, which is described in subsection 3.4. The new layout of the laser-table is shown in Figure 3.1.
The DLpro and TApro lasers have a wavelength near 780 nm. The TA-SHG laser has a side-output with 960 nm and a main-output with 480 nm. After the optical elements the light of our lasers is coupled into optical fibers. Those fibers guide the light to the vacuum chamber on the experiment-table.

3.1.1 Usage of the Lasers

The master laser is used as reference laser for most of the other lasers. A more detailed describtion of the master laser can be read in subsubsection 3.2.1. How the other lasers are locked with respect to the master laser can be read in subsubsection 3.2.2.

The usage of the other lasers is described in the following part:
MOT: The "MOT Cooler" and "MOT Repumper" are used to generate a magneto-optical trap (MOT) [24]. This is the first step in our experiment, where we trap and cool Rubidium atoms in the center of six laser beams. The MOT also needs a magnetic field with a linear gradient in the center of the trap.
RSC: For the Raman Sideband Cooling (RSC) [25, 26] the "RSC Lattice" and "RSC Polarizer" beams are used. With the RSC it is possible to cool the cold atoms in our trap further down.
Optical Pumping: After the trapping and cooling steps we need the "Optical Pumping" beam to prepare the cold atoms for our experiment. By pumping the atoms, they were driven with σ^+ polarized light from $F = 2$ to $F' = 2$, which leads to a population

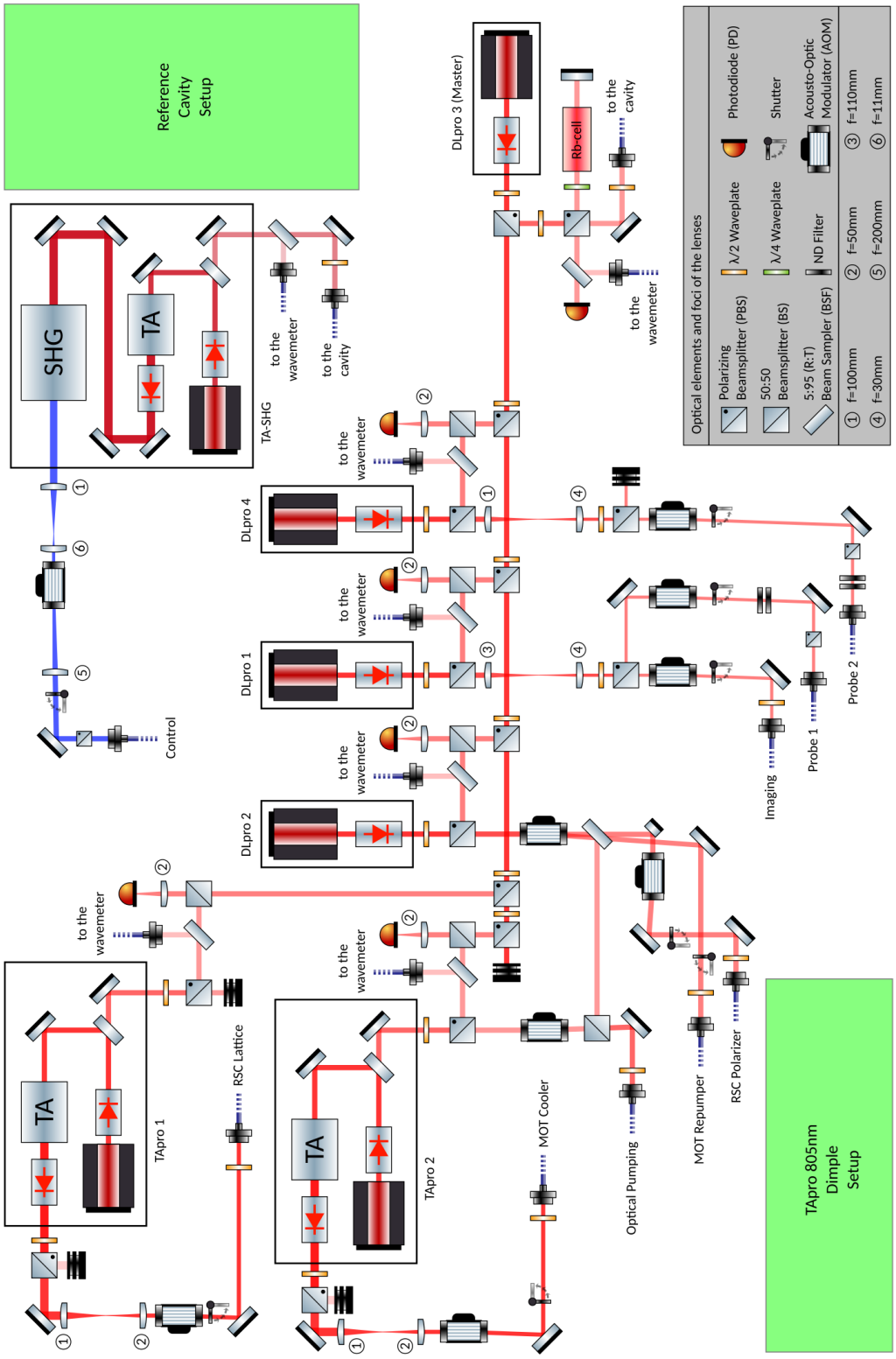

Figure 3.1: Layout of the laser-table in Odense. The laser "DLpro 3" is used as a master laser and stabilized with a reference cavity. All other lasers are stabilized with respect to the master laser. The TA-SHG is also stabilized with the reference cavity. In the dark gray box is the legend for the optical elements and the difference of focal lengths of the lenses. In near future a new laser (TApro 805nm) will be added to the laser-table setup.

of the $5S_{1/2}, F = 2, m_F = 2$ state. With some the MOT Repumper light, the $F = 1$ state is depopulated.
Probe & Control: In our setup we can use two probe beams, "Probe 1" and "Probe 2", and one control beam "Control". Those beams are used to do the Rydberg excitation of our cold atoms.
Imaging: The "Imaging" beam is the last step, which is only used for optimizing the setup or characterization of the cloud. There we take an absorption image of the cold atoms in the trap. The imaging is described in more detail in section 5. We do not use the imaging when we measure Rydberg atoms with the probe beam.

There are two more lasers in our experiment, which are used for the optical dipole trap (ODT) and for the dimple trap. For the ODT we use the above mentioned high power laser, which is set up on the experiment-table and described in the dissertation of H. Gorniaczyk [22]. The setup for the dimple laser will be placed on the laser-table at the already marked position (see Figure 3.1). The principle of the dimple trap is described in the master thesis of C. Zimmer [27] and the new setup will be probably discussed in a thesis in the future.

3.1.2 Optical Elements

The optical elements on the laser-table will be described shortly in the following part:
PBS: The polarizing beamsplitter (PBS) splits the beam into two arms depending on the incoming polarization. The horizontal part of the polarization will be transmitted and the vertical part is reflected. We use such PBS cubes to adjust the laser power in each optical arm of the setup. Therefore we also need a $\lambda/2$ waveplate to adjust the polarization before the PBS.
BS: A beamsplitter (BS) splits the beam with a ratio of 50:50 into the two arms. We use those BS cubes mostly to overlap two beams. This is done for example in front of a photodiode.
BSF: The beam sampler (BSF) is a glass plate which is not coated on one side. This leads to a reflection of approximately 5 % at an angle of incidence of 45 °. In our setup we normally use the BSF to get a beam with low power to measure the wavelength with a wavemeter.
Waveplate: A waveplate changes the polarization of light. There are two common types of waveplates, one is the $\lambda/2$ waveplate and the other is the $\lambda/4$ waveplate. The first one changes the angle of a linear polarization and the second one converts linear polarization into circular polarization and vice versa [28]. On the laser-table we use $\lambda/2$ waveplates in front of PBS cubes to adjust the light power in each of the optical arms.
ND Filter: The neutral density (ND) filter absorbs visible light. The transmission is dependent on the optical density (OD) of the ND filter and almost constant over a large wavelength range. The transmission has a logarithmic dependency on the optical density, $T = 10^{-OD}$. We need ND filters for the "Probe" light to reduce the intensity to the single-photon level.
PD: The photodiode (PD) is a semiconductor chip which is sensitive to light. There are

two designs of PDs, the DC coupled PD and the AC coupled PD. We use AC photodiodes for stabilizing the laser frequencies and a DC photodiode to measure the spectrum of the spectroscopy cell.
Shutter: A shutter is a blade which blocks the light mechanically. Our design is a small flag, which can be rotated by a motor.
AOM: The acousto-optic modulator (AOM) is an optical device, which diffracts light with a sound wave in a crystal. The sound wave acts like a grid where the light is diffracted. The intensity and the diffraction angle are depending on the power and frequency of the sound wave. In our setup we use a frequency of 80 MHz for the 780 nm AOMs and 225 MHz for the 480 nm AOM. As we use the $\pm 1^{st}$ diffraction order after the AOM, we can switch the light on and off by switching the AOM on and off. Important is also that the first order light frequency is shifted by the AOM frequency.

3.2 Laser Locking System

A laser lock is a closed-loop control system to stabilize the frequency of a laser with respect to a reference frequency. In addition to the laser, a system is needed to compare the laser frequency with the reference frequency and thus generate an error signal. The error signal is then processed by a proportional–integral–derivative controller (PID controller) to generate a feedback signal for the laser. By turning on the PID controller the control loop can be closed.
The reference frequency can be an optical transition of an atomic gas. In this case the laser is locked on a spectroscopy signal. Another reference can be an optical cavity. The distance between two high reflective mirrors is fixed and only certain frequency modes fit into the resonator (see subsection 3.4). A third source for a reference frequency can be a radio-frequency oscillator (RF-oscillator).
There are several systems to compare the laser frequency with a reference frequency. In combination with a reference cavity one can use the Pound-Drever-Hall technique [29, 30, 31] to stabilize a laser. The RF-oscillator can be used for the so called delay-line lock or digital phase lock (see subsection 3.3).

3.2.1 Master laser

In our setup the master laser is locked with the Pound-Drever-Hall technique on a reference cavity.
Also possible would be the stabilization of the master laser with a spectroscopy cell. There the laser frequency is stabilized on an atomic transition, in our case a Rubidium transition. One problem with that method is the broad linewdith of the atomic transition, which is limited by the natural linewidth. The natural linewidth is given by the decay time of the used transition. Also the long term stability is not so good, as temperature changes leads to drifts of the transition.
We only use a spectroscopy cell in our setup of the master laser to measure the spectrum of Rubidium by scanning the laser. Thereby we can find the locking transition, which

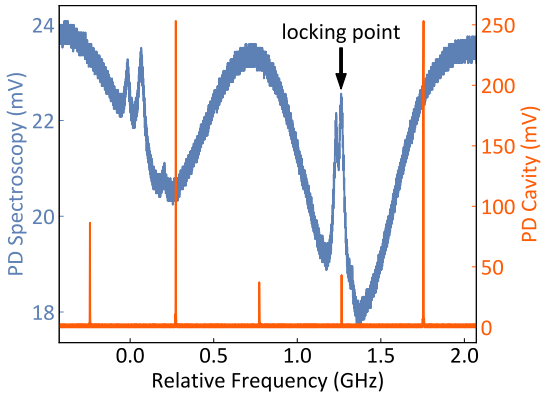

Figure 3.2: Spectrum of Rubidium with the transmission peaks of the reference cavity. The ^{85}Rb $(3 \rightarrow 3)(3 \rightarrow 4)$ crossover transition is marked as locking point. The lower cavity peaks are sidebands, which are modulated on the laser frequency with an electro-optic modulator (EOM). We use the sideband at the marked locking point to stabilize the master laser.

is in our case the ^{85}Rb $(3 \rightarrow 3)(3 \rightarrow 4)$ crossover transition, for our master laser. The stabilization of the frequency and power is done by using the reference cavity (described in subsection 3.4), which is also stable over long times.

A spectrum of Rubidium with the cavity transmission signal is shown in Figure 3.2. We modulate sidebands on the laser frequency, to generate a peak at the locking point. This is done with an electro-optic modulator (EOM), which changes the refractive index of a crystal with an electric field. Thereby the electric frequency is modulated onto the light frequency as sidebands.

3.2.2 Frequency offset lock

As mentioned above, most of the lasers are locked with respect to the master laser with a frequency offset lock, also called beatnote lock. The beatnote is the frequency difference between the two laser frequencies. By overlapping two laser beams onto an AC coupled photodiode the voltage is proportional to:

$$\begin{aligned} V_{PD} &\propto (\cos(\omega_m t) + \cos(\omega_s t))^2 \\ &= 1 + \frac{1}{2}\left(\cos(2\omega_m t) + \cos(2\omega_s t)\right) + \cos([\omega_m + \omega_s]t) + \cos([\omega_m - \omega_s]t)\,, \end{aligned} \tag{3.1}$$

where ω_m is the frequency of the master laser and ω_s is the frequency of the second laser, called slave laser. As the photodiode can only detect frequencies up to 10 GHz, all terms vanishes except the last term with the difference frequency, which is the beat frequency:

$$\omega_{beat} = |\omega_m - \omega_s|\ . \tag{3.2}$$

As ω_m is fixed due to the reference cavity, the frequency ω_s of the slave laser can be stabilized by comparing the beat frequency to a stable RF-oscillator and implement a

feedback to the slave laser.
With the beatnote lock we do not need a reference cavity for each single laser and as we can lock the slave lasers up to 6 GHz away from the master laser, we have a flexible laser system. An overview of the usage of the lasers is shown in Table 3.1, where also the transitions of Rubidium and the corresponding wavelengths are listed. There one can also find the frequency shift caused by the AOM and the frequency offset to the master laser.
The values for the frequency offset in Table 3.1 are the values for a resonant transition, except the RSC Lattice laser. In the experiment we add a detuning to the frequency offset, depending on the usage of the laser. The Probe lasers are blue- or red-detuned to add a detuning to the intermediate state in the Rydberg excitation scheme. Thereby the three level system can be transformed into a two level system by the adiabatic elimination of the intermediate state. The RSC Lattice is far red-detuned to produce a deep trapping lattice in the atom cloud.

The level scheme for Rubidium and the locking transitions of our lasers is shown in Figure 3.3. The master laser is locked to the ^{85}Rb $(3 \to 3)(3 \to 4)$ crossover transition. In the atom cloud we only trap ^{87}Rb in the MOT. Therefore all other lasers are coupled to transitions of ^{87}Rb.

Table 3.1: Usage of the lasers. They are grouped according to the different lasers. The frequencies of the beams are defined by the transitions in Rubidium. The wavelength gives a rough definition of the locking-point. The exact locking-point is given by subtracting the AOM shift from the Rubidium transition. This results in the frequency offset, with respect to the master laser, where the laser has to be locked.

Usage	Laser	Transition	Wavelen. (nm)	AOM (MHz)	Freq. offset (MHz)
Master	DLpro 3	^{85}Rb $(3 \to 3)(3 \to 4)$	780.244		
MOT Cooler	TApro 2	^{87}Rb $2 \to 3$	780.246	$+80$	-1146.4
Optical Pumping	TApro 2	^{87}Rb $2 \to 2$	780.247	-80	-1253.0
MOT Repumper	DLpro 2	^{87}Rb $1 \to 2$	780.233	$+80$	$+5421.7$
RSC Polarizer	DLpro 2	^{87}Rb $1 \to 0$	780.233	-80	$+5352.8$
Imaging	DLpro 1	^{87}Rb $2 \to 3$	780.246	$+80$	-1146.4
Probe 1	DLpro 1	^{87}Rb $2 \to 3$	780.246	$+80$	-1146.4
Probe 2	DLpro 4	^{87}Rb $2 \to 3$	780.246	$+80$	-1146.4
RSC Lattice	TApro 1		780.265	-80	≈ -10000

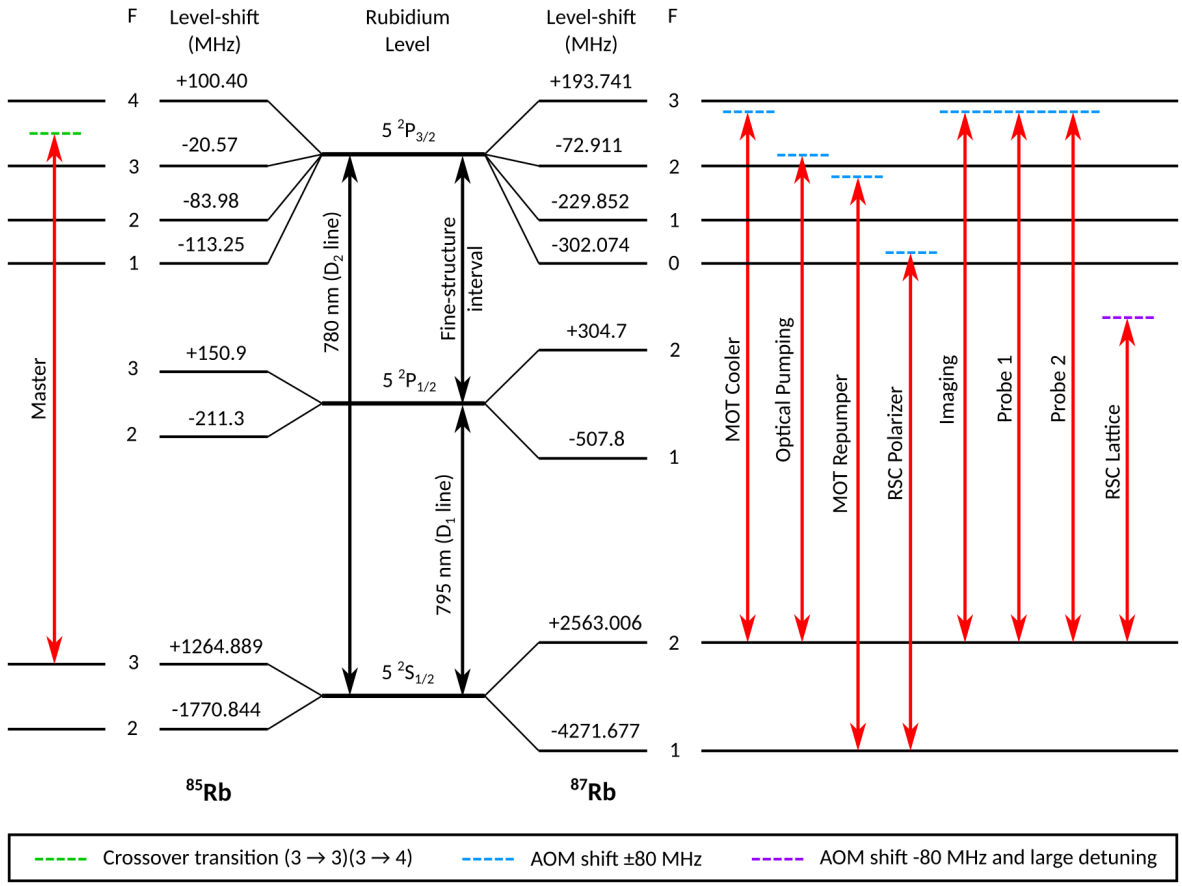

Figure 3.3: Level scheme for Rubidium (adopted from [32]) and locking points of our lasers. We only use lasers close to the Rubidium D_2 line with a wavelength of 780 nm. The frequencies of the lasers are detuned to the Rubidium transitions, because of the frequency shift by the AOM.

3.3 Digital Phase Lock

The digital phase lock is a methode to compare the beat frequency of a frequency offset lock with a stable RF-oscillator. The central component of the digital phase lock is an evaluation board (*Analog Devices* EVAL-ADF4007EBZ1), which compares digitally the frequency and the phase of the two input signals. The idea to use that evaluation board for a digital phase lock of a laser comes from J. Appel [33].

3.3.1 Test setup of the digital phase lock

One project, which was done in Stuttgart, was the setup and characterization of digital phase locks with three lasers in a test setup. Therefore the light of the three lasers were overlapped on three fast AC coupled photodiodes. On each photodiode the light from two lasers is overlapped, so one can measure the beat frequency of the two lasers. In our setup we normally use a beat-frequency of $1 - 2\,\mathrm{GHz}$.

The fast AC coupled photodiodes are self build and can measure frequencies up to 6 GHz. As a next step, the beat frequency of the lasers has to be compared with a reference frequency from a stable RF-oscillator. As a RF-oscillator we use a direct-digital-synthesizer board (DDS-board) with a frequency range from 20 MHz to 240 MHz. Both frequencies, one from the beatnote photodiode and one from the DDS-board, were coupled to a digital phase lock evaluation board. This board compares the two frequencies and outputs an error signal.
As a third step a PID controller generates an error signal for the laser. So the proportional, integration and differentiation part can be adjusted to reach a stable locking loop. The PID controller has a slow and a fast error output, one for the piezo in the laser and one for the laser diode current. The slow output is used to cancel slow drifts of the laser frequency and the fast output to reach a narrow linewidth on a short time scale.

The setup with the three lasers and the three beatnote locks is shown in Figure 3.4. In addition to the three lasers the DLpro laser was also locked with a beatnote lock on the master laser from the main setup. The master laser in turn is locked on the reference

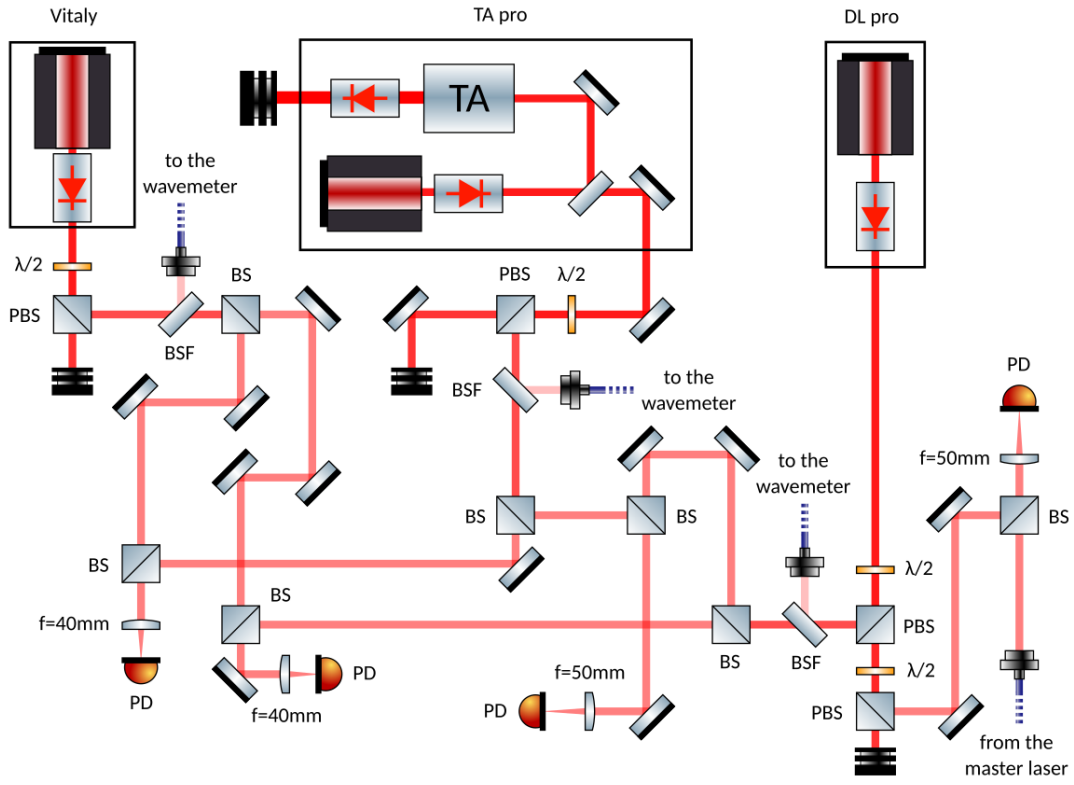

Figure 3.4: Test setup of the three lasers to test the digital phase lock. The light of each laser is split into several arms to overlap always two lasers on one photodiode. To find the beat frequency between two lasers, the wavelength of each laser can be measured with a wavemeter to adjust the laser settings. As the chip of the photodiode is very small, we use a lens to focus the overlapped beams onto the chip. The small chip is necessary to measure signals with a frequency of a few GHz.

cavity.
With this setup it is not possible to measure the absolute linewidth of each laser, therefore each laser has to be locked on a reference cavity. But it is possible to say, that each of the lasers is "following" the frequency of the other laser with a narrow linewidth.

The beat frequency of the DLpro 4 and the master laser was measured over several hours to observe the long time stability. Therefore the spectrum with the beatnote signal was saved every minute. For the evaluation, the beatnote peaks were fitted with a Gaussian function,

$$fit_{\mathrm{G}} = a \cdot e^{-\frac{(f-f_0)^2}{2\sigma^2}} + o\,, \tag{3.3}$$

to get the frequency position and the linewidth of the peaks. The variables in Equation 3.3 are the peak intensity a, the peak frequency f_0, the standard deviation of the Gaussian function σ and an offset o of the signal. The full width at half maximum can be calculated out of σ:

$$\mathrm{FWHM} = 2\sqrt{2\ln 2}\cdot\sigma\,. \tag{3.4}$$

The linewidth of the beatnote peak is the FWHM of the Gaussian function. The resulting frequency drift and linewidth values of the long time measurement are shown in Figure 3.5.

The drift of the beat frequency can have many reasons. One reason can be the PID controller, which can cause a drift of the offset due to a temperature drift. And with a to low gain of the slow output, the piezo, which is connected to the slow output, can not compensate long term drifts. Also the reference frequency of the DDS board can drift over time. Therefore the reference frequency of the DDS board was also measured over a long time (see Figure 3.6). In the end a drift of approximately 300 Hz is not critical for our experiment, as the linewidth of the Rubidium transitions is around 10 times larger

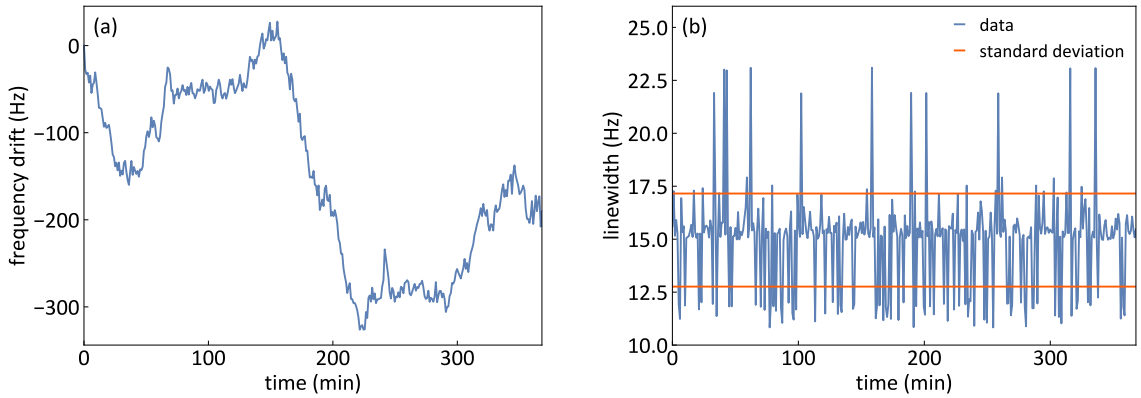

Figure 3.5: Long time measurement of the beatnote signal. The two lasers are the DLpro 4 and the master laser. The beat frequency between them is ≈ 1 GHz. **(a)** Drift of the beat frequency over a few hours. In total the peak drifts around 300 Hz away from the initial position. **(b)** Linewidth of the beatnote peak over a few hours. The two lines are the standard deviation of the signal. The mean value of the linewidth is 22.0 Hz and the standard deviation is 2.4 Hz.

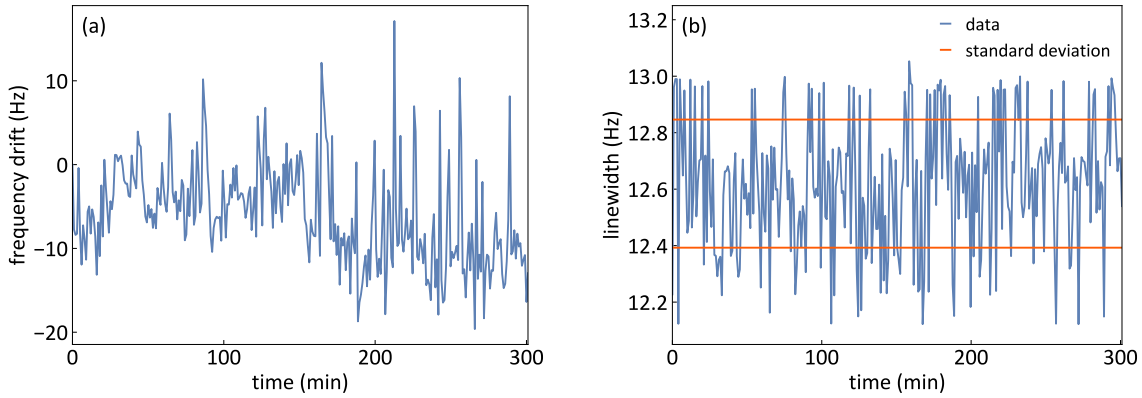

Figure 3.6: Long time measurement of the reference frequency of the DDS board. In this case the frequency was set to 120 MHz. **(a)** Drift of the reference frequency over a few hours. After 5 hours the peak drifted maximal 20 Hz. **(b)** Linewidth of the reference peak over a few hours. The mean linewidth is 19.2 Hz and the standard deviation is 3.5 Hz.

[34]. As the frequency of the 780 nm light is at around 384 THZ, the drift of 300 Hz is a deviation of 7.813×10^{-13}.

Also critical for the experiment is the linewidth of the lasers. As mentioned above with the setup in Figure 3.4 it is not possible to measure the linewidth of each individual laser. But it is possible to measure the linewidth of the beatnote lock, which tells one how narrow one laser "follows" the other laser. In the long time measurement one can see, that the linewidth is always below 30 Hz, so the laser stayed in lock over the measurement time. By calculating the standard deviation of the linewidth we can evaluate a range for the lock linewidth, which is 22.0 ± 2.4 Hz. To measure the linewidth of the laser, one need a different setup.

With the long time measurement of the reference frequency of the DDS board we can say, that the reference is almost stable. In Figure 3.6 one can observe only a small drift of the frequency peak. The drift of 20 Hz is probably caused by noise of the electronics. Also the linewidth of 19.2 Hz is already at the resolution limit of the spectrum analyzer, which is 10 Hz. So the peak drift and the linewidth of the DDS board is very small and narrow, so it is a stable reference source.

The lasers in our setup should be stable on both time scales. So we want a good long term stability of the frequency and power, as well as a narrow linewidth of the laser frequency and power.

3.3.2 Principle of the digital phase lock

The analog input signal is converted by the evaluation board into a digital square pulse. This is done with the beat signal and with the reference signal. Additional the reference signal is divided by a factor R and the beat signal by a factor N. The factor R is fixed to 2, while the factor N can be set via jumpers (jumper N1 and N2) on the evaluation

board to 8, 16, 32 or 64. In the end the board will compare:

$$\frac{f_{ref}}{2} = \frac{f_{beat}}{N} \,. \tag{3.5}$$

With a maximum reference frequency of 240 MHz, the maximum beat frequency can be around 7.5 GHz.

A dual flip-flop circuit on the board compares the frequency and phase of the two signals. The frequency difference will cause a jump from low to high voltage (0...5 V or 0...3 V, depending on jumper LK1) depending on the sign of the frequency difference. The phase difference between reference and beat signal causes a small change in the error output. The point were the two fractions in Equation 3.5 have the same value is called locking-point were the beat frequency is driven to.
There is already a PI stage on the evaluation board, but in our setup we bypass this stage with a wire and only use a capacitor and a resistor at the error output. The capacitor (47 nF) and the resistor (150 Ω) in series have to connect the signal path and ground of the error output (called "VTUNE" on the evaluation board). In Figure 3.7 one can see the two SMD components.

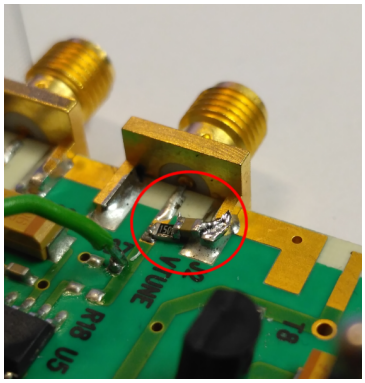

Figure 3.7: Capacitor 47 nF and resistor 150 Ω at the error output.

To see how the lock is working, one can compare the beatnote signal of a free-running

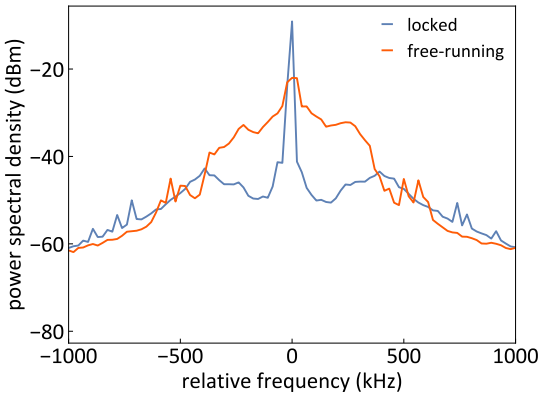

Figure 3.8: Comparison of the free-running DLpro 1 laser with the phase locked DLpro 1 laser. The frequency of the beatnote signal is at ≈ 1.146 GHz. The measurement was done with a span of 10 MHz and a resolution of 1 kHz. In this plot we show only the signal around the main peak, as the outer parts of the two signals are the same. The linewidth of the free-running laser is broader than the linewidth of the locked laser, which is given by the resolution of this measurement.

and a phase locked laser. In Figure 3.8 one can see the difference between the free-running and the phase locked laser. The peak of the free-running laser is broader and lower then the peak of the locked laser. Not visible is the fact, that the frequency of the peak is drifting a lot, while the position of the locked laser is almost stable. The datapoints for the beatnote signals were averaged over 30 scans. The problem with the data of the free-running laser is the large drift of the peak (2.9 MHz in 30 s), so the data has to be shifted to overlap the peaks. The center frequency of the free-running laser can drift more than 5 MHz away in only a few minutes.

3.3.3 Comparison to the delay-line lock

The other system to stabilize the frequency of a laser in our setup is the delay-line lock. At the delay-line lock the reference frequency is produced by a voltage-controlled oscillator (VCO). By mixing the beat and the reference frequency one gets the sum and the difference of the two frequencies. The sum is cut away by a low-pass filter. After a splitter one path is delayed with a longer cable. The delayed and not delayed signals were mixed again. With a second low-pass filter only a non-oscillating cosine term remains. By changing the reference frequency it is possible to tune the zero-crossing of the cosine output signal, which is used as error signal.
In comparison with the digital phase lock the delay-line lock has several locking points, because of the periodic error output. This can be a disadvantage when the laser is locked by accident to the neighbor locking point. Also the slope of the error signal is different. While the slope of the delay-line lock is given by a cosine (or sinus) function, where the slope increases with increasing length of the delay, the slope of the digital phase lock is an almost step-like jump. This results in a more narrow linewidth of the locked laser. In Figure 3.9 the beatnote signal of the two different locks is shown. The model for the fit of the data consists of a Gaussian function added with a Lorentzian function:

$$fit_{\mathrm{G+L}} = a \cdot e^{-\frac{(f-f_0)^2}{2\sigma^2}} + b \cdot \frac{\frac{1}{2}\Gamma}{(f-f_0)^2 + \left(\frac{1}{2}\Gamma\right)^2} + o\,. \tag{3.6}$$

The intensity of the Lorentzian peak is b and the FWHM is given by Γ. All other variables are the same as in Equation 3.3. In our case we use the Gaussian part of Equation 3.6 to fit the narrow peak and the Lorentzian part to fit the broader "shoulders" of the signal. The linewidth of the beatnote signal is then given by the FWHM of the Gaussian part.

By comparing the two plots in Figure 3.9 it is clearly visible, that the digital phase lock leads to a more narrow linewidth . While the lock with the delay-line lock has a broader linewidth of around 90.2 kHz. As mentioned in subsubsection 3.1.1 the DLpro 1 is used for the Rydberg excitation and has to be as narrow as possible. The TApro 2 is used for the MOT, which has a linewidth of around 6 MHz, so the broader linewidth is no problem.
One advantage of the delay-line lock is the more easy controllable reference frequency. That frequency can be directly adjusted with our computer control by applying a volt-

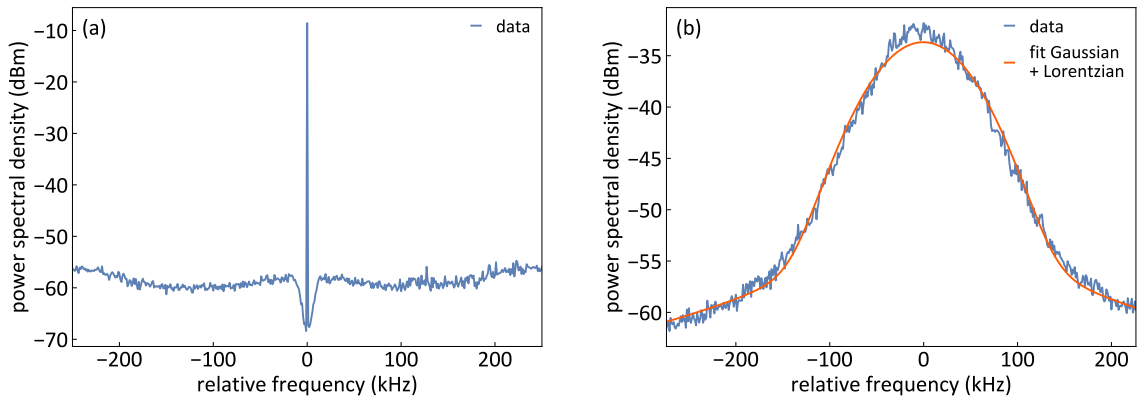

Figure 3.9: Comparison of the digital phase lock with the delay-line lock. The span of the spectrum analyzer is in both cases 500 kHz with a resolution of 100 Hz. The frequency of the beatnote signal is at ≈ 1.146 GHz. **(a)** Beatnote signal of the DLpro 1 and master laser locked with the digital phase lock. The linewidth of the signal is at the resolution of the spectrum analyzer, which is in this case 100 Hz. A zoom in on the signal is shown in Figure 3.10. **(b)** Beatnote signal of the TApro 2 and master laser locked with the delay-line lock. The linewidth has a value of 90.2 kHz.

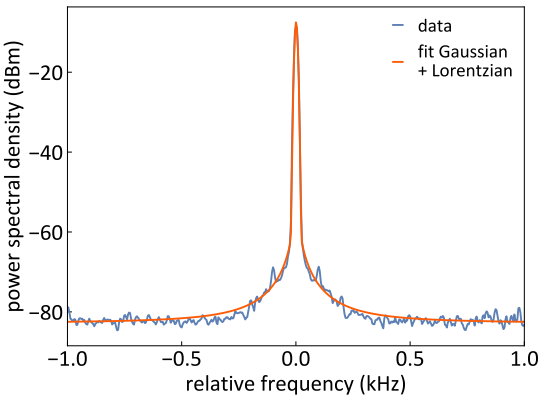

Figure 3.10: Beatnote signal of the DLpro 1 and master laser, measured with a span of 2 kHz and a resolution of 10 Hz. Here it is possible to fit a linewidth of 10.7 Hz, which is at the resolution limit (10 Hz) of the spectrum analyzer. So the actual linewidth of the lock can be smaller.

age to the VCO. For the digital phase lock we need an external reference frequency, as mentioned above, from a DDS board. An improvement for the future could be the combination of the VCO with the digital phase lock. So one could use the VCO to produce the reference frequency, which is applied to the evaluation board.

The beatnote signal of the digital phase lock and the delay-line lock has some "shoulders", which become visible by zooming out and scaning over 10 MHz. In the logarithmic dBm-scale those "shoulders" look as if they were large, but on the linear scale they are

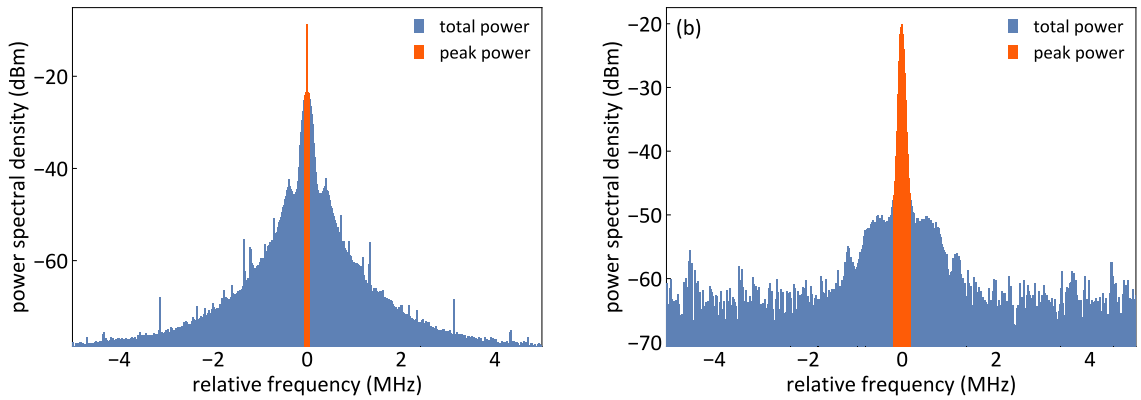

Figure 3.11: Power in the peak of the beatnote spectrum. The peak power (orange area) is divided by the total power (blue + orange area) to determine the percentage power in the peak. The plots are in the logarithmic scale to show the "shoulders" of the peak. The span of the spectrum analyzer was set to 10 MHz with a resolution of 1 kHz. **(a)** The percentage power in the peak is 90.0 % for the DLpro 1 laser. **(b)** The percentage power in the peak is 98.3 % for the TApro 2 laser.

very small. To determine the power in the main peak, the linear signal was integrated over the peak and over the total spectrum. The percentage power in the peak is 90.0 % for the DLpro 1 laser and 98.3 % for the TApro 2 laser. In Figure 3.11 the area of the peak and the total power is shown. The scale is logarithmic to see the signal with the "shoulders" better.

3.4 Reference Cavity

One part of the laser setup is the optical reference cavity. Such a cavity is a resonator with a stable and narrow reference. The narrow reference results from the high finesse of the cavity (see subsubsection 3.4.2). The high finesse is given by two high reflective mirrors. The mirrors are coated with reflection coatings for the wavelength 780 nm and 960 nm. To also have a stable reference the two mirrors are glued on a glass block. That glass block is made out of ultra low expansion (ULE) glass, so the distance between the two mirrors is as stable as possible. The glass block with the mirrors is in a small vacuum tube and also temperature stabilized. A more detailed description of the reference cavity can be found in the master thesis of C. Tresp [35].

3.4.1 Optical Setup for the Cavity

As mentioned before the cavity is used for 780 nm and 960 nm. Therefore the two laser beams have to be overlapped in front of the cavity. This is done with a polarizing beamsplitter (PBS), where the 780 nm light is transmitted and the 960 nm light is reflected because of different polarizations. Thus the 780 nm light is horizontal, in respect to the optical table, polarized and the 960 nm light vertical.

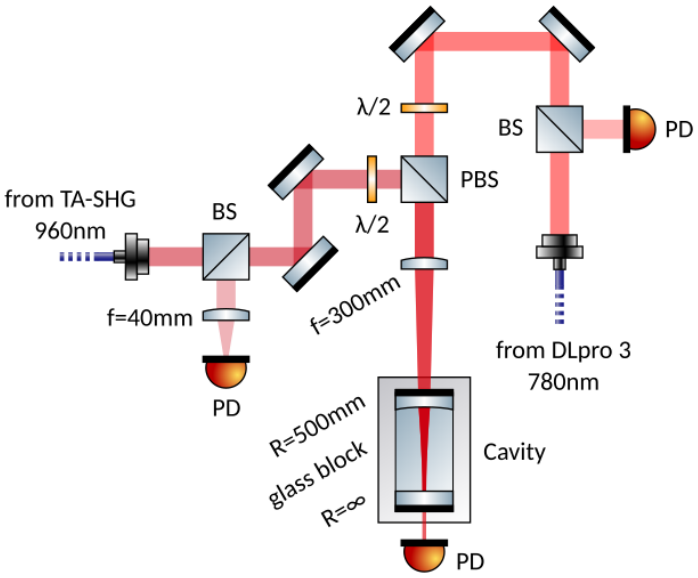

Figure 3.12: Setup in front of the cavity to couple the master and TA-SHG laser into the reference cavity. The photodiode behind the cavity is used to monitor the cavity signal to find the desired cavity mode (see subsubsection 3.4.2). The other two photodiodes are respectively used for the locking loop.

The two photodiodes in the 780 nm and 960 nm arm measure the reflected light of the cavity. As the polarization of the reflected light is not changed, the two photodiodes only see the 780 nm or 960 nm light. The photodiode signal is then transferred into an error signal by using the Pound-Drever-Hall technique. The error signal is processed by a PID-controller, which gives a feedback to the laser and thereby closes the locking loop. With the lens in front of the cavity the light is focused into the cavity. The first mirror is curved with a radius of $R = 500\,\text{mm}$ and the second mirror is planar. The beam shape, which fits into these cavity, is described by a Hermite-Gaussian beam [36, 35].

3.4.2 Finesse of the Cavity

The finesse of a cavity is defined by the free spectral range (FSR) and the full width at half maximum (FWHM) of one cavity mode. The FSR is the frequency difference between two supported cavity modes. A cavity mode is a longitudinal mode with such a wavelength, that fits into the resonator. The length of the cavity has to be a multiple of half the wavelength λ

$$L = q \cdot \frac{\lambda_q}{2}\,. \tag{3.7}$$

The corresponding frequency is given by

$$\nu_q = \frac{c}{\lambda_q} = q \cdot \frac{c}{2L}\,, \tag{3.8}$$

where c is the speed of light. With a given length of the resonator the FSR can be calculated out of the frequency distance between to cavity modes

$$\Delta\nu_{FSR} = \nu_{q+1} - \nu_q = \frac{c}{2L}\,. \tag{3.9}$$

The FWHM of one cavity mode is the linewidth of a single cavity transmission peak in the frequency spectrum. This peak can be fitted with a Lorentzian function to determine the FWHM $\delta\nu$. With the FSR and the FWHM of one cavity peak, it is possible to calculate the finesse of the cavity

$$\mathcal{F} = \frac{\Delta\nu_{FSR}}{\delta\nu}\,. \tag{3.10}$$

With a given reflectivity of the cavity mirrors the Finesse can also be calculated with

$$\mathcal{F} = \frac{\pi\sqrt{R}}{1-R}\,, \tag{3.11}$$

where R is the reflectivity of the mirrors at the used wavelength.

The glass block in our cavity is specified to be $L = 100.1\,\text{mm}$ long. This results in a FSR of $\Delta\nu_{FSR} = 1.497\,\text{GHz}$. With the reflectivity of the mirrors at 780 nm and 960 nm the finesse has a theoretical value of

$$\begin{aligned} R_{780} = 0.99987546 \quad &\rightarrow \quad \mathcal{F}_{780,theo} = 25224\,, \\ R_{960} = 0.99988193 \quad &\rightarrow \quad \mathcal{F}_{960,theo} = 26608\,. \end{aligned} \tag{3.12}$$

A third solution to get the finesse is the measurement of the decay of a cavity mode. Out of the decay time the finesse can be calculated with

$$\mathcal{F} = \tau \cdot \frac{\pi c}{L}\,, \tag{3.13}$$

where τ is the decay time. The cavity mode is decaying because of the reflectivity of the two mirrors. For perfect mirrors, with reflectivity $R = 1$, the light in the cavity would be trapped for ever, but it is not possible to couple light into such a cavity. In reality the mirrors have a reflectivity $R < 1$, which causes a loss of photons after a certain time. Depending on the finesse, which is proportional to the reflectivity, the decay time is longer or shorter.
All in all the finesse can be determined by the FWHM of a cavity mode, or by the reflectivity of the cavity mirrors, or by the decay time of a cavity mode

$$\mathcal{F} = \frac{\Delta\nu_{FSR}}{\delta\nu} = \frac{\pi\sqrt{R}}{1-R} = \tau \cdot \frac{\pi c}{L}\,. \tag{3.14}$$

3.4.3 Measurement of the Finesse

The FWHM of one cavity peak can be measured to calculate the finesse with the FSR and the FWHM. But this is very inaccurate because the width of the transmission peak is varying from measurement to measurement due to the scan of the laser. One has to make many measurements to reduce this error. So we measured the decay time of a cavity mode. Therefore the laser has to be locked to one cavity mode and then kicked out of lock. With a triggered photodiode it is possible to see the transmission of the cavity mode decaying.
In our setup the lasers were locked with the Pound-Drever-Hall technique. The error signal from the Pound-Drever-Hall module is processed by a PID-controller from *Toptica* called *FALC*. To kick the laser out of lock a square pulse with a high level of 100 mV and a width of 200 μs is applied to the second input of the PID-controller. At the same time the photodiode is triggered to measure the decay of the cavity transmission signal on the oscilloscope. The photodiode is terminated with 10 kΩ to have a rise/fall time of $\approx 0.13\,\mu$s to measure the fast decay time.
The measured data for 780 nm and 960 nm are shown in Figure 3.13. The decay was fitted with the model

$$fit_{\text{decay}} = a \cdot e^{-t/\tau}\,, \tag{3.15}$$

where a is a variable to fit the data. The fitted decay times and the resulting finesse, calculated with Equation 3.13, are

$$\begin{aligned} \tau_{780} &= 2.282388\,\mu\text{s} \quad \rightarrow \quad \mathcal{F}_{780,meas} = 20958\,, \\ \tau_{960} &= 2.541323\,\mu\text{s} \quad \rightarrow \quad \mathcal{F}_{960,meas} = 23335\,. \end{aligned} \tag{3.16}$$

By comparing the theoretical (Equation 3.12) and measured (Equation 3.16) finesse one can observe a difference of 4266 for 780 nm and 3273 for 960 nm. This difference can occur because of errors in the measurement or the fit. Also the theoretical value of the

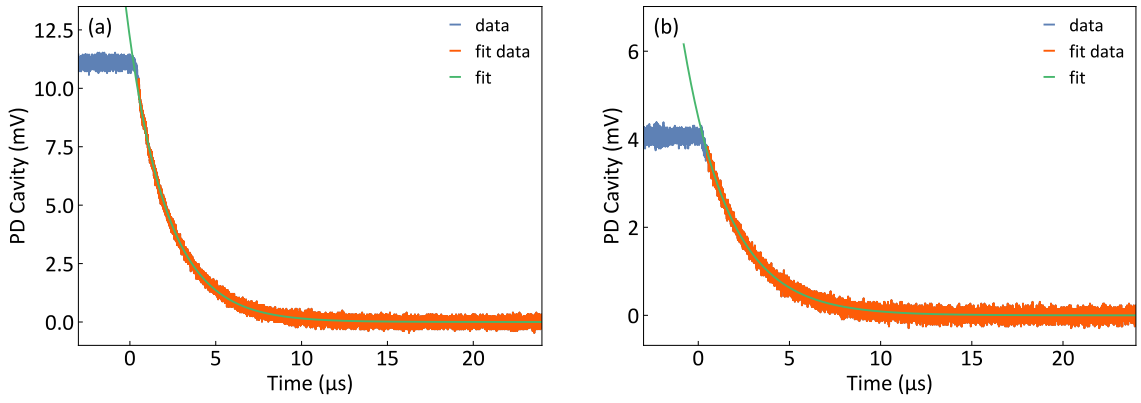

Figure 3.13: Decay of a cavity mode. The data in orange were use for the fit with the model in Equation 3.15. **(a)** The decay time for 780 nm is $\tau_{780} = 2.282388\,\mu$s. **(b)** The decay time for 960 nm is $\tau_{960} = 2.541323\,\mu$s.

finesse can be slightly different, because it is calculated out of the reflectivity of the two mirrors, which can be different from the specifications. All in all with the measurement we showed that our cavity has a finesse above 20000, which means that a cavity mode has a linewidth smaller than $\delta\nu = 75\,\mathrm{kHz}$.

3.4.4 Linewidth of the master laser

The frequency line shape of a single cavity mode can be described with a Lorentzian function. By measuring the fluctuation of the transmission signal of the locked laser, one can estimate the linewidth of that laser. The percentage fluctuation of the signal can be mapped on the Lorentzian cavity mode to determine the frequency fluctuation of the laser. The fluctuation of the signal is asymmetric, because the signal can only get worse in the cavity and not higher than the maximum of the transmission peak. So one has to find the lower bound of the fluctuations to calculate the corresponding laser linewidth. The fluctuations and the corresponding histogram is shown in Figure 3.14. The histogram shows, how often each data value, with a certain y-value, occurs in the data. In this case we normalized the counts for the transmission signal and for the noise of the photodiode. The noise of the PD was shifted to the peak maximum and then subtracted from the transmission data. The resulting curve was used to determine the lower bound of the fluctuations out of the skewness of the transmission signal. The lower

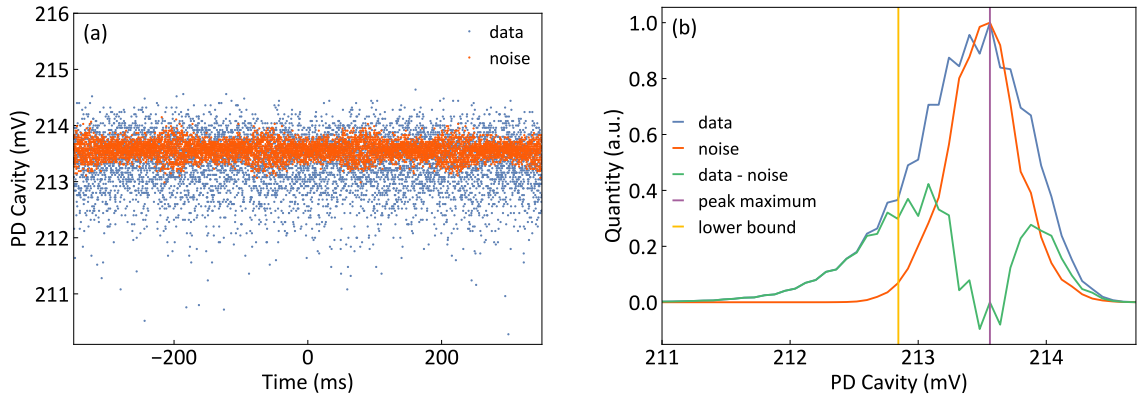

Figure 3.14: Evaluation of the peak fluctuation of the master laser. **(a)** The data of the transmission PD for the locked laser is shown in blue. The electrical noise of the PD, shifted to the maximum of the peak (compare with histogram), is shown in orange. The fluctuation of the laser signal in the upper part is similar to the noise signal. The lower part of the laser shows some runaways, were the transmission signal goes down. **(b)** The normalized histogram of the cavity transmission signal of the master laser is shown in blue. By subtracting the noise (orange) from the data, we observe some remaining counts (green), caused by the skewness of the data. By determining the mean value of the left peak of the remaining counts, we get the lower bound (yellow) of the fluctuations. The right peak and the negative values of the remaining counts should be very small, but here the slope of the data and the noise do not fit perfectly. The peak maximum is marked in purple.

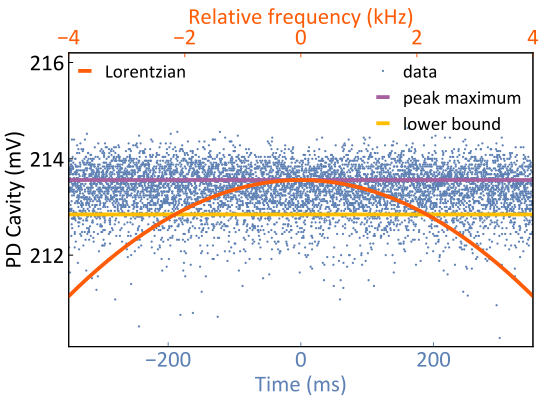

Figure 3.15: Peak fluctuations with peak maximum and lower bound of the fluctuation. The Lorentzian function (with x-axis at the top) has the width of a cavity mode. The intersections of the lower bound with the Lorentzian cavity mode determine the linewidth of the master laser.

bound is given by the mean of the left peak of the remaining counts (see Figure 3.14 (b)). The right peak of the remaining counts can come from stray light on the PD and it may also be that the laser is not exactly locked to the maximum when the error offset is not correct.
By using a Lorentzian function with the width of the cavity mode (75 kHz), the height of the cavity peak and the lower bound of the fluctuations one gets a approximate value for the linewidth of the master laser. With the values in Figure 3.15 the linewidth of the master laser can be determined to 4.3 kHz.
As the digital phase lock has a linewidth of $\approx$ 10.7 Hz, the lasers, locked with that technique, have a laser linewidth with the same order of magnitude as the master laser. So all lasers locked with the digital phase lock in our setup have a linewidth of around 5 kHz. The lasers locked with the delay-line lock are limited by that locking technique, which leads to a laser linewidth of around 100 kHz.

4 Experiment-table Setup

The vacuum chamber is the central element on the experiment-table. The optics around the vacuum chamber had to be disassembled and reassembled for the move from Stuttgart to Odense.
In this chapter I will explain the 3D drawing of our experiment and show the design and setup of a new in vacuum dispenser holder.

4.1 3D Drawing of the Experiment

Before the move to Denmark the experiment setup had to be documented. This was done with the CAD program *Autodesk Inventor* as a three-dimensional assembly. The vacuum chamber and other parts were already there in the 3D drawing. My task was to bring the drawing up to date to have most of the optics in the 3D drawing for the reassembling of the experiment in Denmark. So I looked up the position of the mirrors, beam splitters, waveplates and lenses at the real experiment and placed them at the same position in the 3D drawing. Also the laser beams were illustrated with transparent cylinders to see whether the beams are clipping.
The 3D drawing is a good tool to find the best position for new parts in the experiment setup. Those new parts can be moved around in the drawing, which would be very difficult in the real experiment. One can also measure the distance between different points in the program, which is helpful if the parts are inaccessible in reality.

4.1.1 Version 2 in Stuttgart

The optics and beams for the magneto optical trap (MOT), for the Raman sideband cooling (RSC), for the Dimple, and for the imaging were placed in the 3D drawing. The optics for the probe and control beam and for the optical dipole trap (ODT) are mounted on optics breadboards around the chamber. These breadboards were not disassembled during the move, so it was not necessary to place them in the 3D drawing. A top view with all optical elements and beams is shown in Figure 4.1. This is just an overview how the drawing in the program looks like. In this thesis it is not possible to show all details of the drawing, so I will show the MOT optics and the optics breadboard above the glass cell of the vacuum chamber.

The most important part in the 3D drawing was the MOT optics to rebuild the well working setup around the vacuum chamber. The two beams for the MOT (Cooler and Repumper) were already mentioned in subsection 3.1. Those two beams were overlapped and then enlarged with a telescope, such that the beam diameter is around 1 inch. The large beam is then split into six arms of which four build a rectangle cross in the xy-plane in the glass cell and the other two beams come from the bottom and from the top into the glass cell. The glass cell, where the cold atom cloud is trapped and where the experiments take place, is attached to the metal vacuum chamber. In Figure 4.2 one can see the glass cell and the MOT optics and beams around the glass cell.
With the well documented experiment in the 3D drawing we created a 2D drawing with

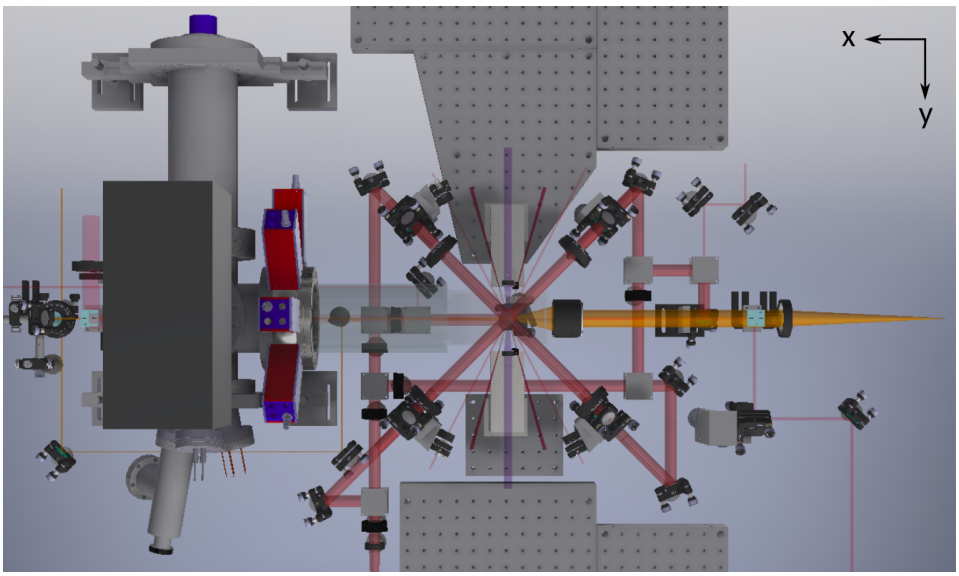

Figure 4.1: Top view on the 3D drawing of the experiment. The color of the beams is not the real light color, they only have different colors to distinguish them. The big red beams are the MOT beams and the yellow beams are the imaging beams. The coordinate system of the experiment, with its origin where the MOT beams cross, is shown in the top right corner of the drawing. Also the optics breadboards in the top and bottom area of the drawing are visible. As mentioned above the optics on these boards is not placed in the 3D drawing so far.

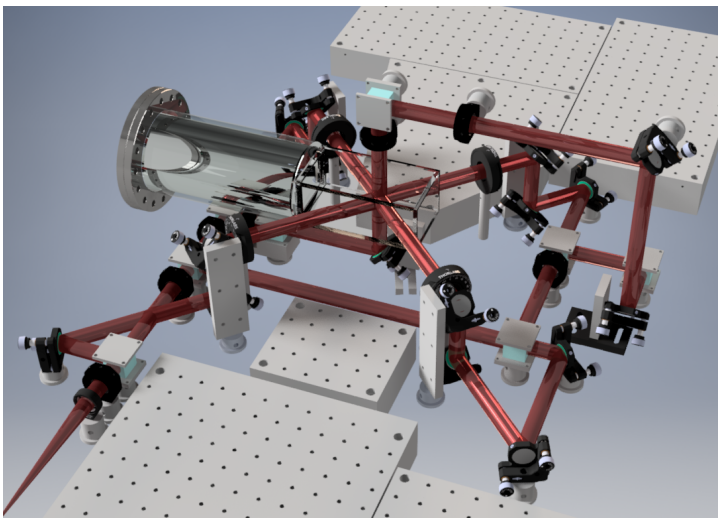

Figure 4.2: View from the side on the MOT optics. In this image one can see how the MOT beam is split into six arms. The MOT light in the glass cell has to be circular polarized, therefore we use $\lambda/4$ waveplates just before the glass cell to generate circular out of linear polarized light. The Rubidium atoms are trapped and cooled in the center of the six MOT beams.

the vacuum chamber and the important MOT optics on it. The 2D drawing with markers for the optic posts was printed, in scale 1:1, on a poster. This plan was then used to place the chamber and the MOT optics precise on the optical table in Odense.

After placing the MOT optics and coils, we managed to trap the first Rubidium atoms in our MOT in Odense. As the Rubidium atoms absorb and emit light at 780 nm in the MOT, it is possible to see the emitted light on a CCD camera. Such a fluorescence image of the MOT in shown in Figure 4.3. In that cloud we are able to trap around 10^7 Rubidium atoms at a temperature of $\approx 45\,\mu$K, the technique to measure the temperature of an atom cloud is described in subsection 5.1.

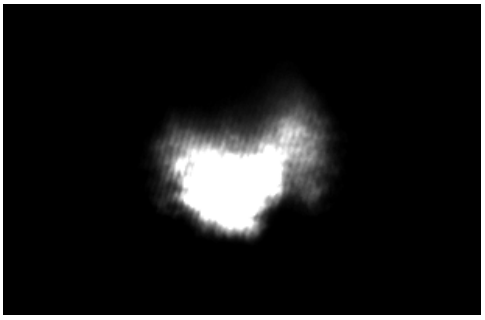

Figure 4.3: Fluorescence of our MOT in Odense. The picture was taken with a Unibrain camera.

4.1.2 Version 3 in Odense

With the help of the 3D drawing it was possible to design a new assembly above the vacuum chamber to replace the vertical breadboard. The new setup consists of a horizontal breadboard for the MOT and imaging optics. With the old vertical breadboard it is difficult to align the optical elements mounted vertically on the breadboard. The new horizontal breadboard has not been built by the end of my master thesis, but after placing it, it will be easier to align the MOT and imaging optics.

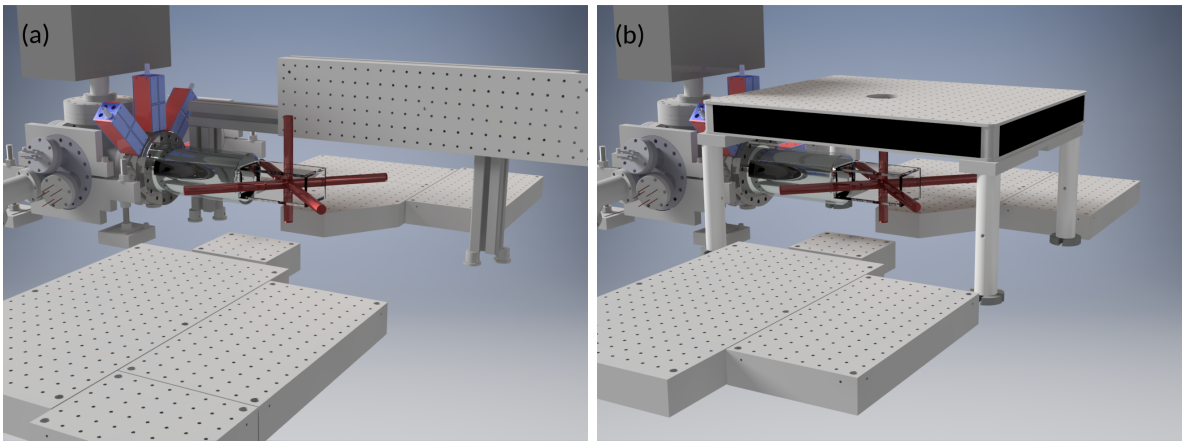

Figure 4.4: Optics breadboards above the glass cell of the vacuum chamber. **(a)** The vertical breadboard is the old assembly of the RQO experiment version 2. **(b)** The new horizontal breadboard has a hole above the middle of the glass cell for the optical access from the top. A custom designed optics holder brings the optical elements through the hole as close to the glass cell as possible. That holder for the MOT optics and the imaging objective is described in section 5.

4.2 Dispenser Setup

The new dispenser holder for six Rubidium dispensers is shown in Figure 4.5. As the feedthrough for the the dispensers has four connections it is possible to drive three pairs of dispensers separately. One contact is ground and the other three are each for one pair of dispensers. The maximum current for one pair is limited by the wire, which can maximally drive 10 A.

The dispenser holder is used in ultra high vacuum ($\approx 10^{-11}$ mbar), so one has to choose

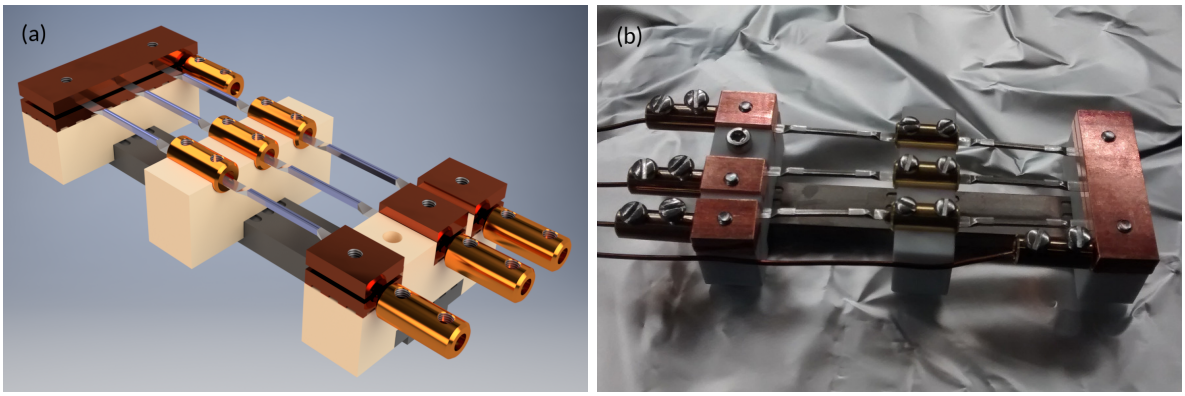

Figure 4.5: Dispenser holder for three pairs of dispenser. **(a)** 3D drawing of the new dispenser holder. **(b)** Photo of the dispenser holder with attached wires.

suitable materials with low outgassing rates. We use the materials stainless steel, copper and Macor. The stainless steel is the base of the holder, the copper is used for the contacts to have a good electric contact between the dispensers and the wire connectors. Macor is a machinable glass-ceramic and used as electrical isolator between the three pairs of dispensers. A difficult thing are threads in Macor, so the design of the holder has to be such, that all threads are in the metal parts.

Another problem in ultra high vacuum is air which is trapped in tiny holes. Such "virtual leaks" can reduce the quality of the vacuum which can be reached. The design of the holder has to take care of contact surfaces were air can be trapped. Therefore the contact surface between the metal and Macor parts should be as small as possible. The solution we choose is shown in Figure 4.6 were the contact surface is reduced by slots.

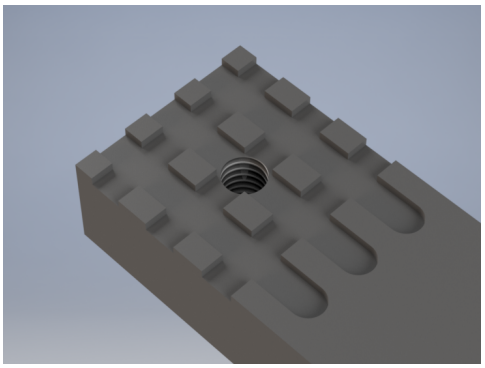

Figure 4.6: Metal surface with slots to reduce the contact surface.

The wire connectors are commercial ones from the *Kurt J. Lesker* company. These beryllium copper inline barrel connectors (FTAIBC134) are stronger than standard copper connectors and enable a good electrical contact. The wire is a Kapton insulated copper wire (FTAK10010) with a diameter of 1 mm and a maximum current load of 10 A.

4.2.1 Rubidium dispenser

The Rubidium dispenser are from the company *SAES Getters*. We use the model RB/NF/4.8/17 FT 10+10 which has an active length of 17 mm. The activation current in the spec-sheet is at 5.3 A, but at that current the dispensers evaporate more Rubidium than we need for our purpose. So we normally drive them with $3 - 4$ A. The first pair of dispensers was used with $4 - 5$ A in order to coat the inside of the chamber with rubidium, which was lost by the opening of the chamber in the course of the move. The other two pairs should be driven with a lower current ≈ 3 A that they last for a long time.

5 Imaging Setup

The last project was the design and characterization of an imaging objective for the RQO experiment. The so called vertical imaging was redesigned in combination with the new optics breadboard, which will be located above the vacuum glass cell.
In this chapter I will describe a standard imaging technique, followed by the design and simulation of the new imaging objective. In the end I will show the characterization of the new vertical imaging objective.

5.1 Absorption Imaging

A standard technique to image a cloud of cold atoms is the so called absorption imaging [37]. This is an optical imaging technique, where the shadow of the atoms is captured.
Therefore we have to take three images with the same camera settings. First we prepare the our sample, then we take an image of the atoms, wait until the atoms are gone, take a second image of the imaging beam and finally measure the stray light without the imaging beam. On the first image one can see a shadow of the atom cloud, because the atoms absorb the imaging light. The optical density (OD) of the atom cloud can be calculated out of the background B, the imaging light L and the shadow of the atoms S

$$OD = \ln\left(\frac{L-B}{S-B}\right). \tag{5.1}$$

The imaging light for the absorption imaging can be blue- or red-detuned to the imaging transition, because at resonance the light would be absorbed and the image would have no graduation in the OD. This measurement was done on resonance, which causes a saturation in the center of the cloud. The absorption imaging is done at the end of the experiment cycle, because the atom cloud is destroyed by the imaging light. Also the dipole trap, in which the atoms are trapped at the end

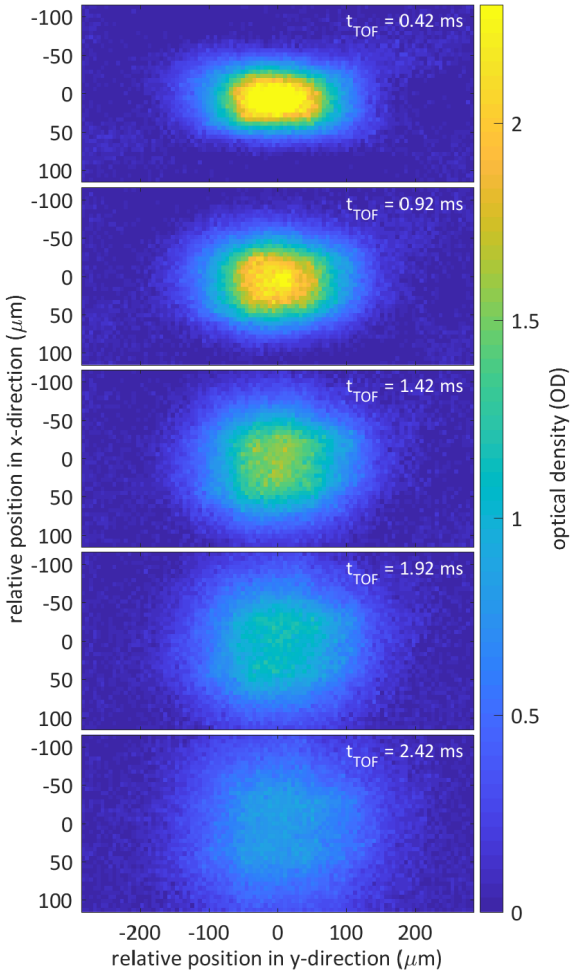

Figure 5.1: TOF-series of the cold atom cloud after all cooling steps. The shown OD of the cloud is calculated out of the three images with Equation 5.1. The x-axis of the images is the y-direction in the experiment and the y-axis is the x-direction.

of the experiment, is turned off just before the imaging.
By varying the time between turning off the trap and imaging the atom cloud, one can measure a time of flight (TOF) series. As the trap is turned off the atom cloud falls down due to gravity. At the same time the cloud expands in all directions, because of the temperature of the atoms and the corresponding velocity.
Out of a TOF series we can determine the number of atoms in the cloud and the temperature of the atoms. As we image our cloud from the top with the vertical imaging, we can determine the temperature in the x- and y-direction of the experiment. The absorption images for a TOF series are shown in Figure 5.1. To calculate the atom number and the temperature, we fit a Gaussian function on the OD in x- and y-direction to measure the expansion of the cloud depending on the TOF. The width of the Gaussian function is given by the initial width σ_0 of the cloud and the width σ_v given by the velocity distribution for a certain TOF, which is visible in the expansion of the cloud

$$\sigma(t) = \sqrt{\sigma_0^2 + \sigma_v^2 t^2}\,. \tag{5.2}$$

The width of the velocity distribution is given by the temperature T of the cloud

$$\frac{\sigma_v^2}{2} = \frac{k_B T}{m}\,, \tag{5.3}$$

where m is the atomic mass of Rubidium and k_B is the Boltzmann constant [38, 27]. For long TOF the width of the cloud is proportional to the velocity distribution. So with a linear fit on the width of the cloud for long TOF we can determine σ_v, which gives us the temperature of the cloud with Equation 5.3.

The width of the cloud in x- and y-direction is shown in Figure 5.2, with a linear fit for long TOF to determine the width of the velocity distribution. The resulting temperatures, calculated with Equation 5.3, in the two directions are $T_x = 2.56\,\mu\text{K}$ and

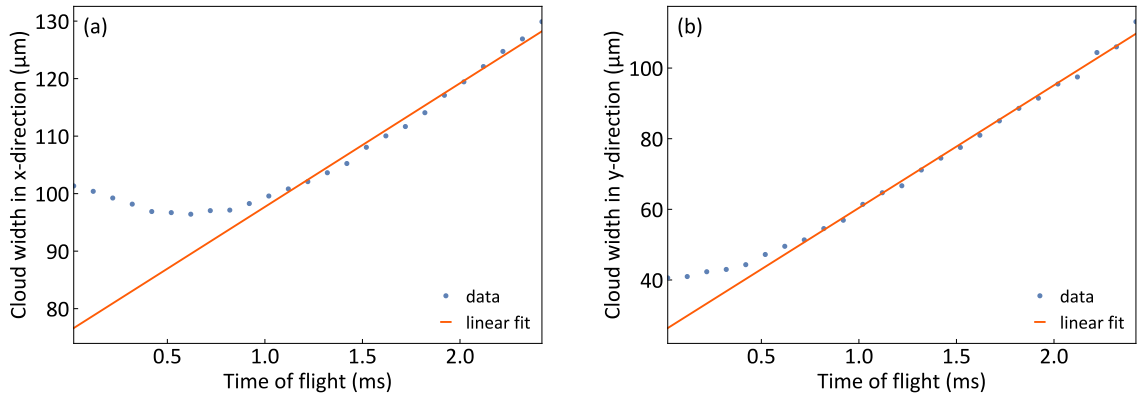

Figure 5.2: Width of the cloud depending on the time of flight. The second half of the data was fitted with a linear fit to determine σ_v. **(a)** Expansion of the width of the cloud in x-direction. The temperature in this direction is $T_x = 2.56\,\mu\text{K}$. **(b)** Expansion in y-direction with a resulting temperature of $T_y = 6.68\,\mu\text{K}$.

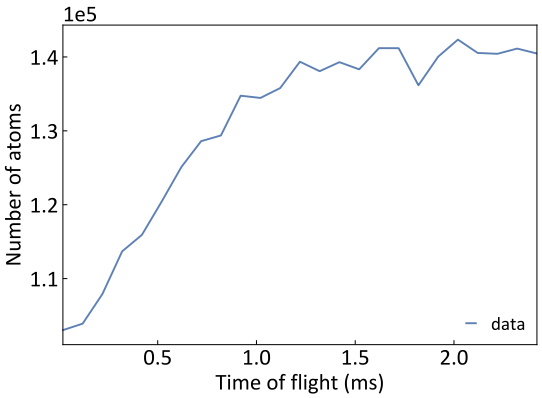

Figure 5.3: Number of atoms in the cloud depending on the TOF. The number is increasing with time, because at the beginning the image is saturated, which gives a wrong value for the atom number. The real number of atoms is given by the last values in the plot, which are around 1.4×10^5 atoms.

$T_y = 6.68\,\mu$K. We can also see, that the expansion is quadratic for short TOF. There is a little dip for short TOF in x-direction, because of saturation effects. The imaging can not resolve the OD for a small dense cloud. This can be improved with a new imaging objective with a higher resolution, which is described in subsection 5.2.
As mentioned above, we can also calculate the number of atoms in the cloud out of the Gaussian line shape of the cloud. In addition, we only need the scattering cross section between imaging light and Rubidium atoms. That is defined by the wavelength λ and the linewidth $\delta\nu$ of the transition, which is used for the imaging, and the detuning Δ of the imaging light. The scattering cross section can be calculated with

$$\sigma_{scat} = \frac{3\lambda^2}{2\pi} \frac{1}{1 + (2\Delta/\delta\nu)^2} \,. \tag{5.4}$$

The number of atoms for a certain TOF is then given by

$$N_{atoms}(t) = OD_{max}(t) \cdot \sigma(t) \cdot \sqrt{\pi} \frac{1}{\sigma_{scat}} \,, \tag{5.5}$$

where $OD_{max}(t)$ is the maximum of the optical density for the respective TOF. The atom number was calculated in x- and y-direction for each TOF image. The mean value of the atom number, depending on the TOF, is shown in Figure 5.3. Good to see in Figure 5.3 is the saturation effect. Because of that saturation, the atom number is not correct for a small dense atom cloud. After a TOF of 1 ms the value for the atom number is almost constant. That value is the real atom number, which is around 1.4×10^5 atoms. With a better imaging system this error can be decreased by increasing the resolution. The new vertical imaging with a higher resolution is described in subsection 5.2.

5.2 Design of the Objective

A high-resolution imaging objective for the RQO experiment was designed by J. Schmidt for the horizontal axis [39]. Here I will describe a high-resolution imaging objective for the vertical axis in the experiment.
The new objective for the vertical imaging was designed with the ray-tracing program *OSLO*. The idea was to increase the resolution of the objective, compared to the old setup, but there are several limitations. For example the MOT optics has to be integrated into the new setup for the vertical imaging, which is limiting the distance to the glass cell. Also the field of view of the objective should be not to small, which means that the magnification should not be to large, otherwise the image would not fit on the chip of the camera. A last point is the diameter of the objective. We decided to use 1 inch optics, because they are cheaper and we have not enough space for 2 inch optics.
For the design of the objective the following parameters are important:
The numerical aperture NA is a number which describes how much light can be collected by the objective. It is defined by the refractive index n of the medium between object and objective (in air $n = 1$) and the angle θ between the optical axis and the outermost ray, which can be collected by the objective. Two times the angel θ defines the light cone, which can be collected by the objective limited by the aperture diameter D. With the focal length f of the objective the numerical aperture can be written as

$$\mathrm{NA} = n \cdot \sin\theta = n \cdot \sin\left[\arctan\left(\frac{D}{2f}\right)\right] \approx n \cdot \frac{D}{2f}\,. \tag{5.6}$$

The resolution of the objective is defined with the so called Airy disk. The radius of the Airy disk q_1 is given by the wavelength λ, the diameter of the aperture D and the focal length f. With Equation 5.6 the aperture diameter and focal length can be replaced by the angle θ

$$q_1 = 1.22\,\frac{f\lambda}{D} \approx 1.22\,\frac{\lambda}{2\sin\theta}\,. \tag{5.7}$$

The radius of the Airy disk is the diffraction limited smallest object distance, which still can be resolved with the objective [28]. This means two point light sources with a distance of the radius of the Airy disk can still be distinguished.
As the objective consists of several lenses, one can calculate the effective focal length of the objective. In our case the optics program calculates the effective focal length of the objective, which can be seen as the focal length of a single thin lens with the same refractive properties. In our imaging system we use an objective to collimate the image and a second lens to focus the image on a camera. With the focal length of the objective f_1 and the focal length of the second lens f_2 we can calculate the magnification of our imaging system

$$M = \frac{f_2}{f_1}\,. \tag{5.8}$$

As mentioned above, with a too large magnification we limit our field of view, as the camera chip is very small.
Another effect in optics are aberrations. Those aberrations are optical errors, which oc-

cur when we look at large angles to the optical axis where the approximation $\sin\theta \approx \theta$ is not valid anymore. The main errors are spherical aberrations, coma, astigmatism, field of curvature and distortion [28]. Those optical errors make the image unclear and can be reduced by optimizing an objective with the optics program. Also the combination of several lenses in an objective can reduce some aberrations compared to a single spherical lens.

The design of the new vertical imaging objective with four lenses was inspired by the objectives presented in a paper of J. D. Pritchard [40]. The combination of a positive meniscus lens, a plano-convex lens, a bi-convex lens and a plano-concave lens allows a smaller focus than a single lens with the same focal length. Also the effect of aberrations is lower. The type of lenses was also copied from the paper of J. D. Pritchard [40], but the focal length of each lens was changed for our needs. We also use 1 inch optics instead of 2 inch optics. The used lenses are standard lenses from *Thorlabs* or *Newport* and the lens tube, in which the lenses are mounted, is also commercial part from *Thorlabs*. This means that the price for the complete objective is cheap, compared to a commercial available objective or customized lenses.
The MOT optics has to be integrated before the imaging objective. That means, that a $\lambda/4$ waveplate and a 1 inch PBS cube have to be in the beam above the glass cell before the objective. After simulating several arrangements of the optics with *OSLO*, we found the setup shown in Figure 5.4. The distance between the glass cell and the $\lambda/4$ waveplate is caused by the magnetic coils above the glass cell, which are not shown in the drawing. The cube has to be that height above the glass cell, because the MOT beam, which comes from the side, has to be above the magnetic coils. The objective with four lenses is, with some tolerance, as close as possible above the cube.
The four lenses from the bottom to the top are in detail:

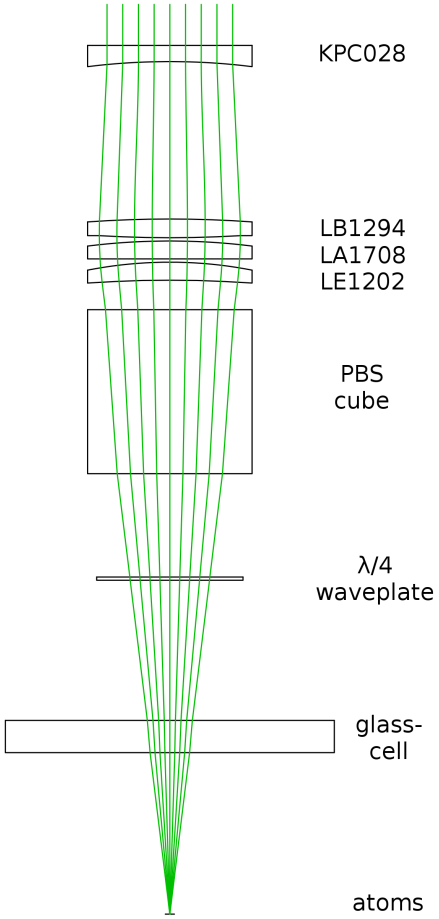

Figure 5.4: Drawing of the new vertical imaging objective. The light from the atoms passes the glass cell, the waveplate and the cube, before it hits the objective. After the objective the image of the atoms is collimated.

- Positive meniscus lens with $f = 200\,\text{mm}$ (*Thorlabs* LE1202-B).
- Plano-convex lens with $f = 200\,\text{mm}$ (*Thorlabs* LA1708-B).

- Bi-convex lens with $f = 175\,\text{mm}$ (*Thorlabs* LB1294-B).
- Plano-concave lens with $f = -200\,\text{mm}$ (*Newport* KPC028AR.16).

The distance between the four lenses was optimized with *OSLO*, such that the root mean square (rms) at the focus is minimal. The focal length of each of the lenses is large, but the resulting effective focal length of the objective has a value of $f_{EFL} = 79.75\,\text{mm}$. With a numerical aperture of NA $= 0.1216$, which is limited by the aperture of the third lens, where the image is the largest, we have an aperture with a half-angle of $\theta = 6.985\,°$. The resolution is given by the radius of the Airy disk, which is $q_1 = 3.91\,\mu\text{m}$. For comparison, the current vertical imaging uses a single lens with $f = 175\,\text{mm}$ with a resolution of $q_1 = 6.61\,\mu\text{m}$.

The four lenses are mounted in a 2 inch long lens tube for 1 inch optics (*Thorlabs* SM1M20). The first three lenses, from the bottom to the top, are combined to one set of lenses with custom made distance rings between them. The fourth lens is mounted separately, such that the distance between the set of lenses and the single lens can be adjusted. The optimized distance between the set and the fourth lens is 24 mm, but the fourth lens can be moved closer to the set, if the image can not be focused. On the other hand, if the distance between cube and objective is larger then 8 mm, the fourth lens should be moved away from the set, such that the objective has to be moved closer to the cube to focus the image. The optimized distance between the lens tube and the cube is 2 mm.
A half cut through the lens tube and the complete assembly of the vertical imaging is

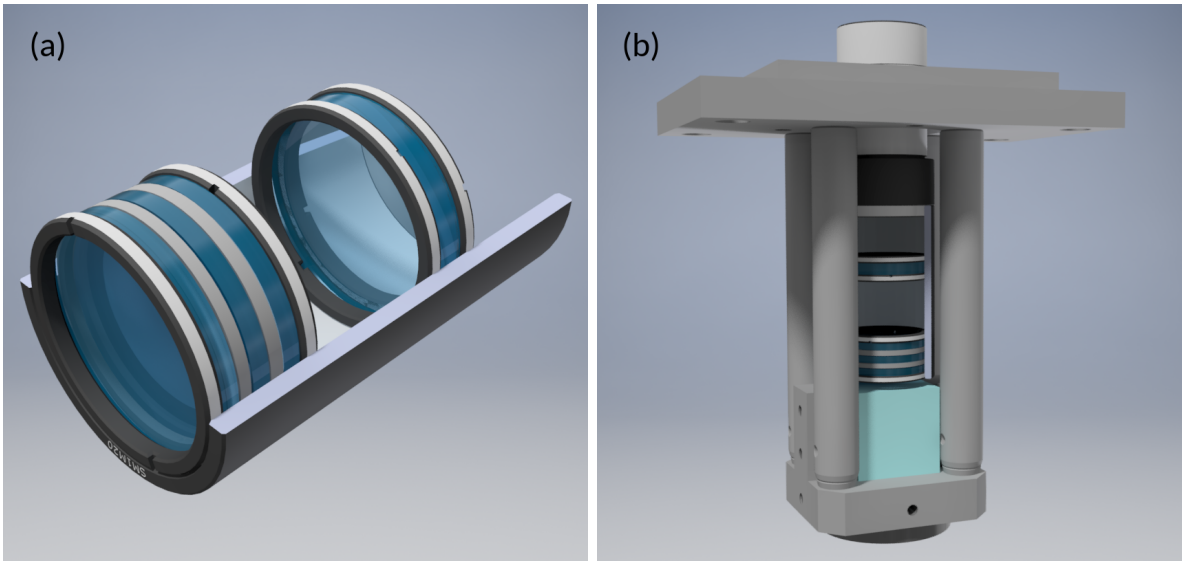

Figure 5.5: 3D drawing of the vertical imaging setup. **(a)** Half cut through the lens tube to see how the lenses are mounted. The last lens can be screwed out from the back, to adjust the distance between the first three lenses and the fourth lens. **(b)** Complete holder for the vertical imaging with waveplate holder (black part at the bottom) and cube (blue) for the MOT beam. The assembly can be inserted into the hole in the new horizontal breadboard above the glass cell (see Figure 4.4).

shown in Figure 5.5. The lens tube with the objective inside is screwed with a adjustable lens tube (*Thorlabs* SM1V15) into a metal plate, such that the tube can be moved up or down by screwing the tube out or in. With that mechanism the image can be focused. When the focus was found the position can be locked with a locking ring (*Thorlabs* SM1NT).
The vertical imaging setup is completely defined by the lens data from *OSLO*, which are shown in Table 5.1. The curvature of the surfaces is not shown, as we used predefined lenses, where the curvature is already set. The refractive index of the materials is defined in the program via the type of glass. In *OSLO* the optimization of the objective was done backwards. So the object is a point light source with a large diameter very far away, such that the beam is collimated when it hits the first surface of the objective. The distance of the focus behind the glass cell was taken from the 3D drawing and was fixed in *OSLO*. For the optimization only the four lenses could be moved to minimize the focus diameter.

Table 5.1: Lens data with all optical surfaces and their thickness on the optical axis. These are the values which describe the optical system in *OSLO*. Normally the program uses the curvature of each surface, but in this case we used predefined lenses where only the name is shown in the column "Element". The PBS cube, the $\lambda/4$ waveplate and the glass cell have only flat surfaces. The position and the aperture radius of the MOT-coils is also listed in this table, but that aperture is not the limiting one. The surface called "Aperture stop" is the limiting surface, where the image is clipping at the distance ring, which has an inner diameter of 0.86 inch.

Surface	Element	Thickness [mm]	Aperture radius [mm]	Glass
Object	–	1.0000e+20	8.7269e+17	Air
1	NKPC028	2.500000	12.700000	N-BK7
2		24.381423	12.700000	Air
3	TLVISLB1294	2.900000	12.700000	N-BK7
Aperture stop		0.500000	10.950000	Air
5	TLVISLA1708	2.780000	12.700000	N-BK7
6		0.500000	12.700000	Air
7	TLVISLE1202	2.790000	12.700000	N-BK7
8		4.569877	12.700000	Air
9	PBS cube	25.400000	12.700000	N-SF1
10		16.000000	12.700000	Air
11	$\lambda/4$ waveplate	0.500000	11.300000	Quartz
12		5.600000	11.300000	Air
13	aperture of MOT-coils	16.100000	14.500000	Air
14	glass cell	5.000000	25.400000	Quartz
15		0.000000	25.400000	Air
Image	–	25.000000	0.696625	

5.3 Performance Simulation

With the above mentioned Optics Software for Layout and Optimization (*OSLO*) it is possible to simulate single rays going through the objective. By sending a bundle of rays, equally spread over the first optical surface, through the objective, we can simulate the focus in the image plane. In such a spot diagram we can observe the behavior of defocussing and aberrations, which are caused by the objective.

By sending the rays parallel to the optical axis through the optics, we get a spot diagram shown in Figure 5.6. The green dots are the position of the rays after traveling through the objective and due to some aberrations the green spot in the circle with 5 μm focus shift looks smaller then the one at zero focus shift. But the expansion of the beam at positive shift is larger, so the optimized focus is at zero focus shift. That effect is probably caused by the optimization algorithm of the optics program. In the end the rays, which are calculated via linear optics, are all inside the white circle, which is the above mentioned Airy disk. That means that the focus is diffraction limited also for a shift of $\pm 10\,\mu$m out of the focus. Also at a shift of $\pm 30\,\mu$m all rays are inside the Airy

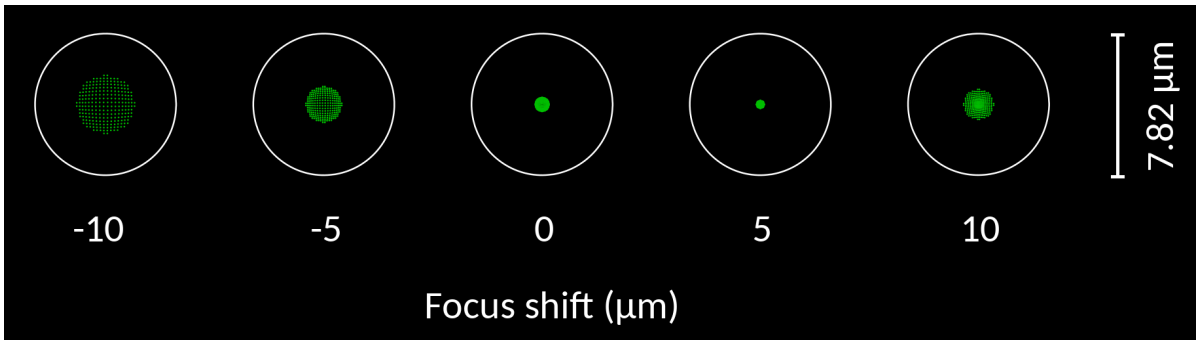

Figure 5.6: Spot diagram for rays parallel to the optical axis. The white circle is the Airy disk with a diameter of $2q_1 = 7.82\,\mu$m, which marks the diffraction limit. A focus smaller then the Airy disk can not be resolved. As all rays, marked with green dots, are inside the Airy disk, also for a defocus of $\pm 10\,\mu$m, the objective is diffraction limited and reaches the calculated resolution given by the radius of the Airy disk.

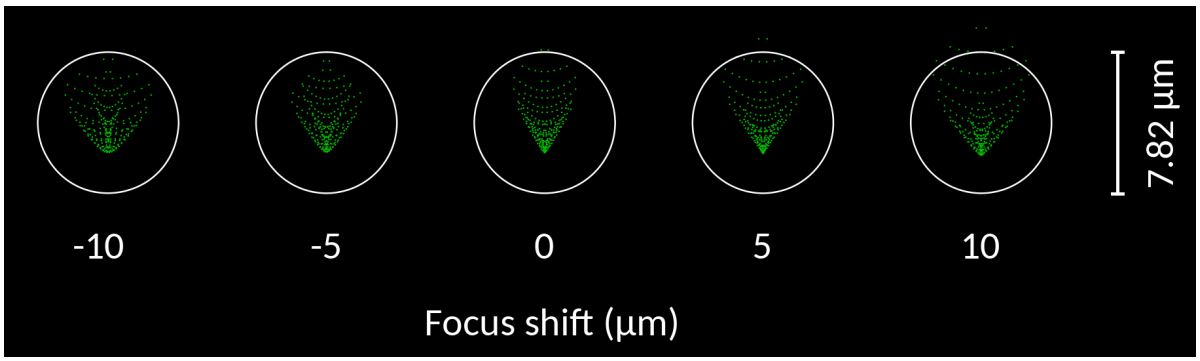

Figure 5.7: Spot diagram for rays tilted by 0.5 ° to the optical axis. Some rays (green dots) are outside the Airy disk (white circle) for a focus shift of $\pm 10\,\mu$m. The comatic aberration leads to a triangular distribution of the dots.

disk and therefore diffraction limited.
When the rays are tilted by 0.5 ° some aberrations occur in the spot diagram. For a tilt of the objective or rays the dominant effect is the comatic aberration. That effect shifts the inner or outer rays sideways. The resulting spot diagram is shown in Figure 5.7.

Another property of the objective is the modulation transfer function (MTF) which describes the contrast of the image depending on the resolution of the object. The MTF is part of the optical transfer function (OTF) which also contains optical phase informations. For our purpose the MTF is enough to see the performance of our objective, anyway we can not measure the optical phase with our camera. Therefore one needs a Shack-Hartmann sensor to measure the wavefront to get the phase informations.
The contrast or modulation of an object or image is defined with the minimal and maximal intensity of the object or image. The modulation can be calculated with [28]

$$\text{Modulation} = C = \frac{I_{max} - I_{min}}{I_{max} + I_{min}} \,. \tag{5.9}$$

When we take an object with black and white stripes we have a contrast of 100 %. By taking an image of that object with a lens or an objective we lose contrast, as the edges between black and white smear out. The width on which the transition from black to white smears out is dependent on the lens or objective. With a smaller object size, which means smaller distance between the black and white stripes, the width on which the transition smears out is more and more dominant. In the end, at a very small object size, the contrast goes to zero and the black and white stripes of the object are one gray area in the image. The effect, just described, is shown in Figure 5.8, where the contrast

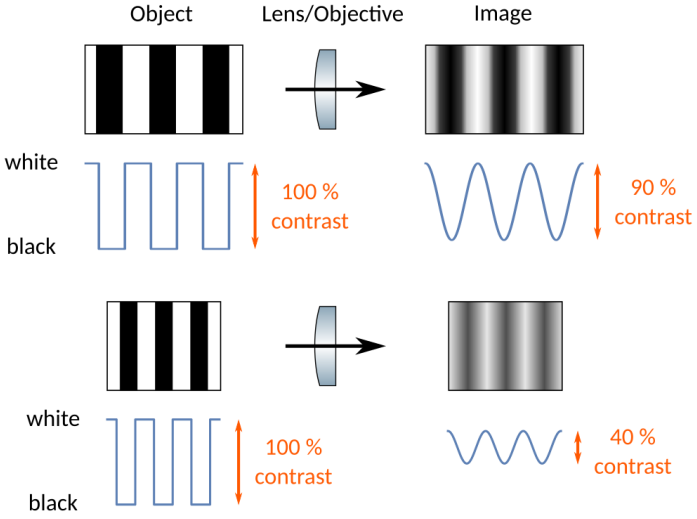

Figure 5.8: Contrast of the object and image for different resolutions (adopted from [41]). The contrast of the object can be described with a square function between black and white, while the contrast of the image is a sinus function when the width of the transition is larger than the width of a stripe.

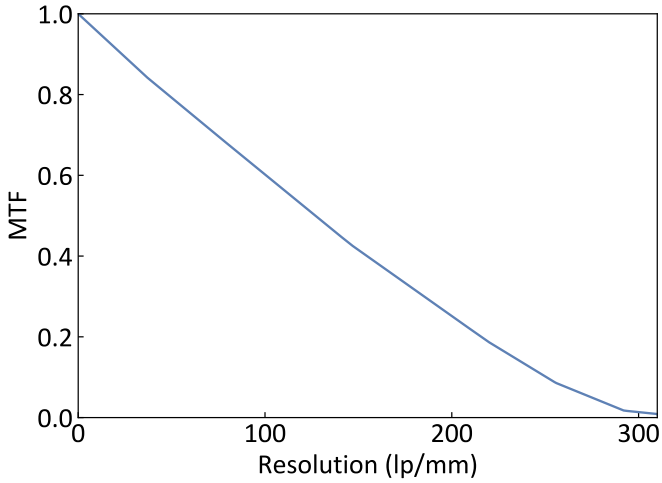

Figure 5.9: MTF of the vertical imaging objective. The curve shows how the contrast is going down with increasing resolution. The cut-off frequency is at 310.45 lp/mm.

of the image for two resolutions is shown.
The MTF describes how the modulation decreases with increasing resolution. The resolution is given in line-pairs per millimeter (lp/mm), which is also called spatial frequency. The point where the MTF reaches zero modulation is called cut-off frequency. For our vertical imaging objective the cut-off frequency is at 310.45 lp/mm. The MTF calculated with *OSLO* is shown in Figure 5.9.

5.4 Characterization of the Objective

To characterize the objective one can use a resolution test target. We use the 1951 USAF resolution chart, which has stripe pattern in the horizontal and vertical direction. Those pattern are sorted in groups and elements. The resolution of the pattern is increasing with increasing group and element number. The minimum linewidth of our resolution chart is 0.78 μm, which is group 9 element 3. The resolution can be calculated with the group and element number

$$\text{Resolution (lp/mm)} = 2^{group+(element-1)/6}\,. \tag{5.10}$$

The calculated resolution of the objective is 3.91 μm, which is the same as group 7 element 1 with 3.91 μm.

The test setup, which was used to characterize the objective, is shown in Figure 5.10. The laser is running at a wavelength of 780.246 nm, which is later used for the absorption imaging. The beam is magnified with a telescope. To destroy the coherence of the laser light, we use a rotating diffuser. The self-build diffuser consists of a computer fan without flaps and a transparent documents foil, which has a structure on one side, such that it is not clear. A circle with the diameter of the fan housing is cut out from the foil and glued on the motor of the fan. The beam can shine through the rotating foil

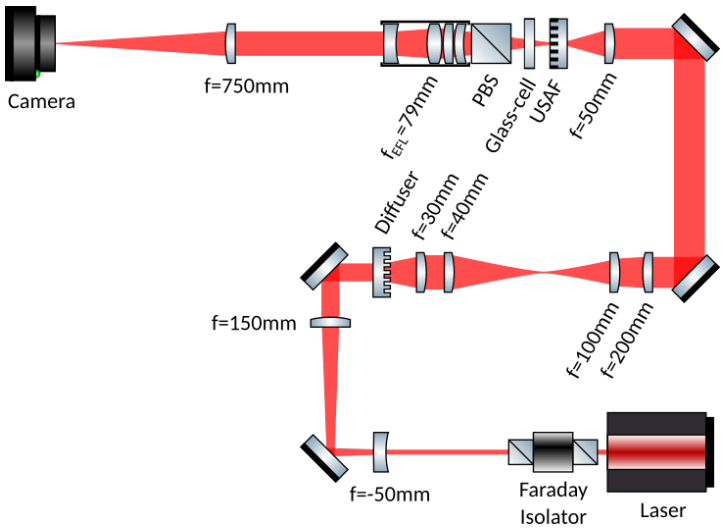

Figure 5.10: Setup to characterize the performance of the imaging objective. The coherence of the laser ligth is destroyed with a rotating diffuser. The diffuse light is focused on the USAF resolution chart. The image is collected with the new objective and focused on the camera with a lens, which has a long focal length.

in the gap, where the flaps have been. The diffuse light, which is also very divergent, is collimated as good as possible with four lenses. The large incoherent beam is focused with a 50 mm lens on the USAF resolution chart. That lens has to be moved around to find the best illumination of the resolution chart, such that diffraction effects vanishes. The resolution chart is mounted on a 3D translation stage with an accuracy of 10 μm. The image of the resolution chart passes a glass-plate, which is similar to the vacuum glass cell, and a 1 inch PBS cube before it is collimated by the objective. The collimated image is focused with a 750 mm lens onto a camera. We used the *Raspberry Pi* camera module v2 with a 3280 $\times$ 2464 px chip and a specified pixel size of 1.12 μm $\times$ 1.12 μm.
To prove and calibrate the pixel size of the camera we used the USAF resolution chart without any optics. The chart was placed in front of the camera chip and illuminated with a LED flashlight from a few meters away. We took a picture of group 0 element 1 in vertical and horizontal direction. As we know the width of the stripes on the resolution chart, we can count the pixels in one stripe and determine the pixel size. The measurement leads to a pixel size of 1.114 μm $\times$ 1.119 μm, which is in good agreement with the specification.
As the focal length of the second lens, which is used for focusing the image on the camera, is $f_2 = 750$ mm and the effective focal length of the objective is $f_1 = 79.75$ mm, we have a magnification, calculated with Equation 5.8, of $M = 9.4$. That means that an object with 0.12 μm is imaged on one pixel and an object with 3.91 μm is imaged on $\approx$ 36 pixels. The magnification in the experiment setup will not be that high, as we probably use a 200 mm lens, resulting in a magnification of 2.5.

The picture of the USAF resolution chart, taken with the *Raspberry Pi* camera module v2 in the test setup, is shown in Figure 5.11. The picture was cut into small pictures,

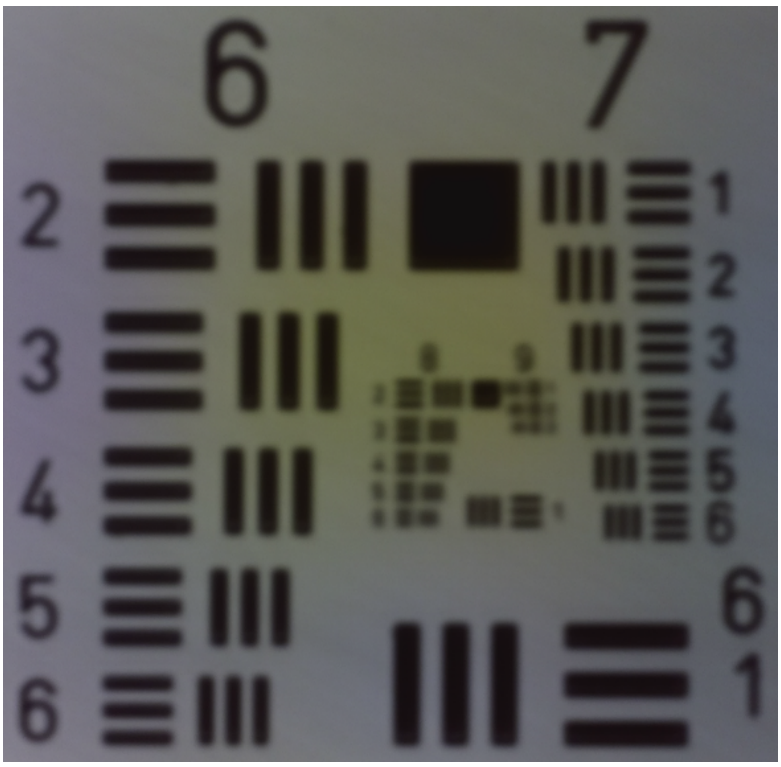

Figure 5.11: Picture of the 1951 USAF resolution chart. The element 1 in group 7 is still visible, which corresponds to a linewidth of 3.91 μm. The last element in group 7 has a low contrast, but is also resolvable. The picture was taken with the *Raspberry Pi* camera module v2 in the test setup.

where only one horizontal or vertical pattern with three dark stripes is on it.

The horizontal or vertical stripes in one pattern where averaged along the long axis of the stripe to get the contrast between dark and bright. Therefore the pictures with one pattern were converted into a 8-bit gray-scale (0$\hat{=}$dark, black, 255$\hat{=}$bright, white). The minimum intensity is given by the lowest data point, while the maximum intensity between the three black stripes was determined with a Sinus function. That Sinus function is only used to determine the maximum intensity for the contrast and is not a model to describe the stripe pattern. With I_{min} and I_{max} the contrast C can be calculated with Equation 5.9. An exemplary evaluation of the stripe pattern is shown in Figure 5.12 for the element 1 in group 6 in vertical direction.

The contrast was calculated for all elements in group 6 and 7. As a systematic error for I_{min} and I_{max} we chose $\Delta I_{min} = \Delta I_{max} = 10$ on the 8-bit gray-scale. With that error one can calculate the error of the contrast ΔC with the propagation of uncertainty

$$\begin{aligned} \Delta C &= \frac{\partial C}{\partial I_{max}} \cdot \Delta I_{max} + \frac{\partial C}{\partial I_{min}} \cdot \Delta I_{min} \\ &= \frac{2I_{min}}{(I_{max} + I_{min})^2} \cdot \Delta I_{max} - \frac{2I_{max}}{(I_{max} + I_{min})^2} \cdot \Delta I_{min} \,. \end{aligned} \tag{5.11}$$

One problem during that measurement were the settings of the camera. We used the

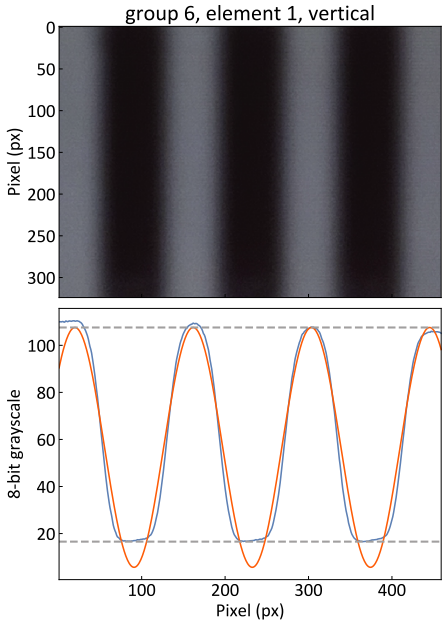

Figure 5.12: Evaluation of the pattern in group 6 element 1 in vertical direction. The picture at the top is averaged along the long axis of the stripes to get the plot at the bottom. The data is shown in blue and the Sinus function in orange. The minimum and maximum intensity are marked with dashed gray lines.

camera in an automatic mode, where we could not set parameters like the shutter speed, the exposure time, the gamma value or the brightness of the camera. Without that values it is hard to reproduce any measurement.

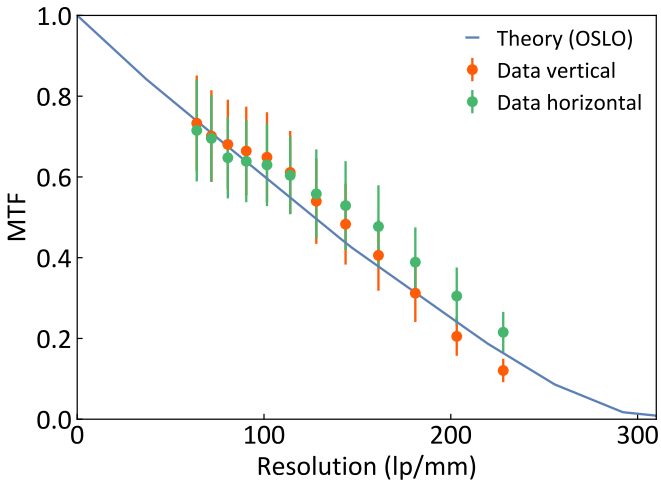

Figure 5.13: Modulation transfer function of the vertical imaging objective. The theoretical values (blue) were calculated with *OSLO*. The measured values (vertical data in orange and horizontal data in green) for the contrast are in good agreement with the theoretical simulation.

With the contrast and the resolution of our patterns in group 6 and 7, we can compare these measurements with the theoretical MTF calculated with *OSLO*. The measured data points for vertical and horizontal patterns are shown in Figure 5.13 with error bars for the contrast and the theoretical MTF.
The vertical and horizontal data are within the error bar of each other, so the objective has the same performance in both directions. The data points are also close to the theoretical curve, so we reached the predicted performance of the vertical imaging objective.

6 Conclusion and Outlook

In the course of this Master thesis, a third generation Rydberg quantum optics apparatus was setup.
Within the move from Stuttgart to Odense, the RQO experiment was changed. One change was the installation of a new laser locking system, the so called digital phase lock. The linewidth of the digital phase lock is at 10.7 Hz, which is at the resolution limit of our spectrum analyzer. In comparison, the linewidth of the before use delay-line lock is at 90.2 kHz. Also part of the laser stabilization is the reference cavity. Our cavity has a measured finesse of $\mathcal{F}_{780,meas} = 20958$ respectively $\mathcal{F}_{960,meas} = 23335$. These values are close to the theoretical values calculated with the specified reflectivity of the mirrors $\mathcal{F}_{780,theo} = 25224$ and $\mathcal{F}_{960,theo} = 26608$. Our master laser locked with the reference cavity has an estimated linewidth of 4.3 kHz. As the linewidth of the digital phase lock is narrow, the slave lasers locked with that technique have also a linewidth of approximately 5 kHz.
On the actual experiment we only had minor changes. A new part inside the vacuum chamber is the Rubidium dispenser holder. That new designed assembly contains three pairs of Rubidium dispensers.
The new vertical imaging objective with a numerical aperture of NA = 0.1216 and a effective focal length of $f_{EFL} = 79.75$ mm has a resolution, defined by the radius of the Airy disk, of $q_1 = 3.91\,\mu$m. The design and simulations were done with the optics program *OSLO*. Out of the simulation of the spot diagrams we can say that our design is diffraction limited in the focus and also at a focus shift of $\pm 30\,\mu$m. The objective was characterized in a test setup with the USAF 1951 resolution chart. The resulting contrast values for different resolutions are in good agreement with the theoretical modulation transfer function.

Some parts of the setup for the new vertical imaging were not there at the end of my thesis. So a project for the future will be the installation of the new breadboard above the glass cell of the vacuum chamber. Then the objective can be installed and adjusted with the custom designed holder. With the new imaging the absorption images will be better, so the characterization of the cloud of atoms, like temperature or number of atoms, will be more precise. This will contribute to a better understanding of the experiments, done with the cloud of cold Rubidium atoms, in our RQO experiment.
All in all the reconstruction of the RQO experiment allows us to measure the interaction between single photons and Rydberg atoms. Based on our recent paper [20], which deals with a single superatom, we would like to create several superatoms, which can interact with each other via single photons.

References

[1] I. Friedler, D. Petrosyan, M. Fleischhauer, and G. Kurizki. "Long-range interactions and entanglement of slow single-photon pulses". In: *Phys. Rev. A* **72** (4 2005), p. 043803.

[2] J. D. Pritchard, D. Maxwell, A. Gauguet, K. J. Weatherill, M. P. A. Jones, and C. S. Adams. "Cooperative Atom-Light Interaction in a Blockaded Rydberg Ensemble". In: *Phys. Rev. Lett.* **105** (19 2010), p. 193603.

[3] A. V. Gorshkov, J. Otterbach, M. Fleischhauer, T. Pohl, and M. D. Lukin. "Photon-Photon Interactions via Rydberg Blockade". In: *Phys. Rev. Lett.* **107** (13 2011), p. 133602.

[4] T. F. Gallagher. *Rydberg atoms*. Cambridge University Press, 1994.

[5] T. Baluktsian, B. Huber, R. Löw, and T. Pfau. "Evidence for Strong van der Waals Type Rydberg-Rydberg Interaction in a Thermal Vapor". In: *Phys. Rev. Lett.* **110** (12 2013), p. 123001.

[6] C. Carr, R. Ritter, C. G. Wade, C. S. Adams, and K. J. Weatherill. "Nonequilibrium Phase Transition in a Dilute Rydberg Ensemble". In: *Phys. Rev. Lett.* **111** (11 2013), p. 113901.

[7] A. Urvoy, F. Ripka, I. Lesanovsky, D. Booth, J. P. Shaffer, T. Pfau, and R. Löw. "Strongly Correlated Growth of Rydberg Aggregates in a Vapor Cell". In: *Phys. Rev. Lett.* **114** (20 2015), p. 203002.

[8] T. Kazimierczuk, D. Fröhlich, S. Scheel, H. Stolz, and M. Bayer. "Giant Rydberg excitons in the copper oxide Cu_2O". In: *Nature* **514** (7522 2014), pp. 343 –347.

[9] M. D. Lukin, M. Fleischhauer, R. Cote, L. M. Duan, D. Jaksch, J. I. Cirac, and P. Zoller. "Dipole Blockade and Quantum Information Processing in Mesoscopic Atomic Ensembles". In: *Phys. Rev. Lett.* **87**.3 (June 2001), p. 037901.

[10] T. Peyronel, O. Firstenberg, Q.-Y. Liang, S. Hofferberth, A. V. Gorshkov, T. Pohl, M. D. Lukin, and V. Vuletic. "Quantum nonlinear optics with single photons enabled by strongly interacting atoms". In: *Nature* **488** (7409 2012), pp. 57–60.

[11] O. Firstenberg, T. Peyronel, Q.-Y. Liang, A. V. Gorshkov, M. D. Lukin, and V. Vuletic. "Attractive photons in a quantum nonlinear medium". In: *Nature* **502** (7469 2013), pp. 71–75.

[12] D. Tiarks, S. Schmidt, G. Rempe, and S. Dürr. "Optical phase shift created with a single-photon pulse". In: *Science Advances* **2**.4 (2016). eprint: `http://advances.sciencemag.org/content/2/4/e1600036.full.pdf`.

[13] H. Gorniaczyk, C. Tresp, J. Schmidt, H. Fedder, and S. Hofferberth. "Single-Photon Transistor Mediated by Interstate Rydberg Interactions". In: *Phys. Rev. Lett.* **113** (5 2014), p. 053601.

[14] A. Reiserer and G. Rempe. "Cavity-based quantum networks with single atoms and optical photons". In: *Rev. Mod. Phys.* **87** (4 2015), pp. 1379–1418.

[15] A. F. van Loo, A. Fedorov, K. Lalumière, B. C. Sanders, A. Blais, and A. Wallraff. "Photon-Mediated Interactions Between Distant Artificial Atoms". In: *Science* **342**.6165 (2013), pp. 1494–1496.

[16] J. Petersen, J. Volz, and A. Rauschenbeutel. "Chiral nanophotonic waveguide interface based on spin-orbit interaction of light". In: *Science* **346**.6205 (2014), pp. 67–71.

[17] A. Sipahigil, R. E. Evans, D. D. Sukachev, M. J. Burek, J. Borregaard, M. K. Bhaskar, C. T. Nguyen, J. L. Pacheco, H. A. Atikian, C. Meuwly, R. M. Camacho, F. Jelezko, E. Bielejec, H. Park, M. Lončar, and M. D. Lukin. "An integrated diamond nanophotonics platform for quantum-optical networks". In: *Science* **354**.6314 (2016), pp. 847–850.

[18] M. K. Tey, Z. Chen, S. A. Aljunid, B. Chng, F. Huber, G. Maslennikov, and C. Kurtsiefer. "Strong interaction between light and a single trapped atom without the need for a cavity". In: *Nat Phys* **4** (12 2008), pp. 924–927.

[19] C. Tresp, C. Zimmer, I. Mirgorodskiy, H. Gorniaczyk, A. Paris-Mandoki, and S. Hofferberth. "Single-Photon Absorber Based on Strongly Interacting Rydberg Atoms". In: *Phys. Rev. Lett.* **117** (22 2016), p. 223001.

[20] A. Paris-Mandoki, C. Braun, J. Kumlin, C. Tresp, I. Mirgorodskiy, F. Christaller, H. P. Buechler, and S. Hofferberth. "Free-Space Quantum Electrodynamics with a single Rydberg superatom". In: *ArXiv* 1705.04128 (2017).

[21] I. Mirgorodskiy, F. Christaller, C. Braun, A. Paris-Mandoki, C. Tresp, and S. Hofferberth. "Electromagnetically induced transparency of ultra-long-range Rydberg molecules". In: *Phys. Rev. A* **96** (1 2017), p. 011402.

[22] H. Gorniaczyk. "Single Photon Transistor mediated by electrically tunable Rydberg-Rydberg Interactions". Dissertation. Universität Stuttgart, Dec. 2016.

[23] C. Tresp. "Rydberg polaritons and Rydberg superatoms - Novel tools for quantum nonlinear optics". Dissertation. Universität Stuttgart, Feb. 2017.

[24] E. L. Raab, M. Prentiss, Alex Cable, Steven Chu, and D. E. Pritchard. "Trapping of Neutral Sodium Atoms with Radiation Pressure". In: *Phys. Rev. Lett.* **59** (23 1987), pp. 2631–2634.

[25] , C. Chin, A. J. Kerman, and S. Chu. "Degenerate Raman Sideband Cooling of Trapped Cesium Atoms at Very High Atomic Densities". In: *Phys. Rev. Lett.* **81** (26 1998), pp. 5768–5771.

[26] S. E. Hamann, D. L. Haycock, G. Klose, P. H. Pax, I. H. Deutsch, and P. S. Jessen. "Resolved-Sideband Raman Cooling to the Ground State of an Optical Lattice". In: *Phys. Rev. Lett.* **80** (19 1998), pp. 4149–4152.

[27] C. Zimmer. "Single-Photon Gates Mediated by Single-Blockade-Sized Rydberg Medium". Master thesis. Universität Stuttgart, May 2016.

[28] E. Hecht. *Optics*. 4th ed. San Francisco: Addison-Wesley, 2002.

[29] R. W. P. Drever, J. L. Hall, F. V. Kowalski, J. Hough, G. M. Ford, A. J. Munley, and H. Ward. "Laser phase and frequency stabilization using an optical resonator". In: *Applied Physics B* **31**.2 (1983), pp. 97–105.

[30] E. D. Black. "An introduction to Pound–Drever–Hall laser frequency stabilization". In: *American Journal of Physics* **69**.1 (2001), pp. 79–87.

[31] F. Christaller. "Aufbau und Charakterisierung von einem Lasersystem zur schmalbandigen Anregung von Rydberg-Atomen". Bachelor thesis. Universität Stuttgart, Sept. 2015.

[32] A. Banerjee, D. Das, and V. Natarajan. "Precise fine-structure and hyperfine-structure measurements in Rb". In: *ArXiv* physics/0209019 (2002).

[33] J. Appel, A. MacRae, and A I Lvovsky. "A versatile digital GHz phase lock for external cavity diode lasers". In: *Measurement Science and Technology* **20**.5 (2009), p. 055302.

[34] R. Löw, H. Weimer, J. Nipper, J. B. Balewski, B. Butscher, H. P. Büchler, and T. Pfau. "An experimental and theoretical guide to strongly interacting Rydberg gases". In: *Journal of Physics B: Atomic, Molecular and Optical Physics* **45**.11 (2012), p. 113001.

[35] C. Tresp. "A setup for highly precise excitation and detection of Rydberg atoms". Master thesis. Universität Stuttgart, Oct. 2012.

[36] B. Saleh and M. C. Teich. *Fundamentals of Photonics*. 2nd ed. Wiley, 2007.

[37] T. Pyragius. "Developing and building an absorption imaging system for Ultracold Atoms". In: *ArXiv* 1209.3408 (2012).

[38] T. M. Brzozowski, M. Maczynska, M. Zawada, J. Zachorowski, and W. Gawlik. "Time-of-flight measurement of the temperature of cold atoms for short trap-probe beam distances". In: *Journal of Optics B: Quantum and Semiclassical Optics* **4**.1 (2002), p. 62.

[39] J. Schmidt. "Generation of non-classical light using ultra-cold Rydberg ensembles". Master thesis. Universität Stuttgart, Oct. 2014.

[40] J. D. Pritchard, J. A. Isaacs, and M. Saffman. "Long working distance objective lenses for single atom trapping and imaging". In: *Review of Scientific Instruments* **87**.7 (2016), p. 073107.

[41] Edmund Optics, Inc. *Introduction to Modulation Transfer Function*. `https://www.edmundoptics.com/resources/application-notes/optics/introduction-to-modulation-transfer-function/`. Oct. 2017.

Acknowledgment / Danksagung

Mein Dank gilt Allen, die mich bei meiner Arbeit unterstützt haben. Vor allem möchte ich mich bedanken bei:

Prof. Dr. Sebastian Hofferberth und **Prof. Dr. Tilman Pfau**, dass ich die Möglichkeit bekommen habe am 5. Physikalischen Institut meine Masterarbeit zu schreiben und im Zuge dessen einige Monate ins Ausland gehen konnte.

Prof. Dr. Peter Michler, dass er den Mitbericht meiner Arbeit übernommen hat.

Dr. Christoph Tresp, **Dr. Asaf Paris Mandoki** und **Christoph Braun**, die mir immer mit Rat und Tat beiseite standen und auch zum Gelingen dieser Arbeit beigetragen haben.

Der RQO/NQO Gruppe, für die gute Zusammenarbeit und gegenseitige Unterstützung innerhalb der Gruppe, auch abseits der Physik.

Allen anderen Mitarbeitern am 5. Physikalischen Institut, die mich schon seit meiner Bachelorarbeit begleiten.

I would also like to thank the students and employees at the University of Southern Denmark (SDU), whom I met during my stay in Odense.